**Final Report
for the period
August 1985 to
March 1986**

Infrared Optical Property Measurement Techniques:
Definition and Preliminary Design

**DTIC
ELECTE
S JUL 3 1 1986
D   D**

July 1986

Authors:
T. E. Parker
D. I. Rosen
W. T. Rawlins

Physical Sciences, Inc.
Research Park
P.O. Box 3100
Andover, MA 01810

PSI-060/TR-559
F04611-85-C-0060

Approved for Public Release

AD-A170 426

prepared for the: **Air Force
Rocket Propulsion
Laboratory**

Air Force Space Technology Center
Space Division, Air Force Systems Command
Edwards Air Force Base,
California 93523-5000
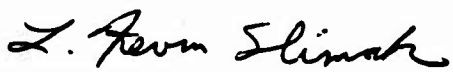
86 7 31 016

DTIC FILE COPY

NOTICE

When U.S. Government drawings, specifications, or other data are used for any purpose other than a definitely related government procurement operation, the government thereby incurs no responsibility nor any obligation whatsoever, and the fact that the government may have formulated, furnished, or in any way supplied the said drawings, specifications, or other data, is not to be regarded by implication or otherwise, or conveying any rights or permission to manufacture, use, or sell any patented invention that may in any way be related thereto.

FOREWORD

This final report on Infrared Optical Property Measurement Techniques was prepared by Physical Sciences, Inc., Andover, MA, in fulfillment of contract F04611-85-C-0060. Project Manager for the Air Force Rocket Propulsion Laboratory was Lt James A. Misener.

This technical report has been reviewed and is approved for publication and distribution in accordance with the distribution statement on the cover and on the DD Form 1473.

JAMES A. MISENER, 1Lt, USAF
Project Manager

L. KEVIN SLIMAK
Chief, Interdisciplinary Space
Technology Branch

FOR THE DIRECTOR

DAVID L. NEURAUTER, Lt Col, USAF
Chief, Propulsion Analysis Division

AD-A170 436

REPORT DOCUMENTATION PAGE

1a. REPORT SECURITY CLASSIFICATION UNCLASSIFIED	1b. RESTRICTIVE MARKINGS
2a. SECURITY CLASSIFICATION AUTHORITY	3. DISTRIBUTION/AVAILABILITY OF REPORT Approved for Public Release; Distribution
2b. DECLASSIFICATION/DOWNGRADING SCHEDULE	is Unlimited
4 PERFORMING ORGANIZATION REPORT NUMBER(S) PSI-060/TR-559	5. MONITORING ORGANIZATION REPORT NUMBER(S) AFRPL-TR-86-034

6a. NAME OF PERFORMING ORGANIZATION Physical Sciences Inc.	6b. OFFICE SYMBOL (If applicable)	7a. NAME OF MONITORING ORGANIZATION Air Force Rocket Propulsion Laboratory
6c. ADDRESS (City, State and ZIP Code) Research Park P.O. Box 3100 Andover, MA 01810		7b. ADDRESS (City, State and ZIP Code) AFRPL/DYSO Edwards AFB, CA 93523-5000
8a. NAME OF FUNDING/SPONSORING ORGANIZATION	8b. OFFICE SYMBOL (If applicable)	9. PROCUREMENT INSTRUMENT IDENTIFICATION NUMBER F04611-85-C-0060

8c. ADDRESS (City, State and ZIP Code)	10. SOURCE OF FUNDING NOS.			
	PROGRAM ELEMENT NO.	PROJECT NO	TASK NO	WORK UNIT NO
11 TITLE (Include Security Classification) INFRARED OPTICAL PROPERTY MEASUREMENT TECHNIQUES: DEFINITION..	65502F	3148	00	EB

12. PERSONAL AUTHOR(S)
Parker, T.E., Rosen, D.I., and Rawlins, W.T.

13a. TYPE OF REPORT Final	13b. TIME COVERED FROM 85/8 TO 86/03	14. DATE OF REPORT (Yr., Mo., Day) 86/7	15 PAGE COUNT 87

16. SUPPLEMENTARY NOTATION

17 COSATI CODES			18 SUBJECT TERMS (Continue on reverse if necessary and identify by block number)
FIELD	GROUP	SUB. GR	Infrared Optical Properties, Index of Refraction, Aluminum
21	08		Oxide, Rocket Exhaust Particles, Absorption Coefficients,
			Shock Tube, Polarization Ratio, Mie Scattering,

19. ABSTRACT (Continue on reverse if necessary and identify by block number) in crown oxvs

An experimental design for the determination of the complex indices of refraction for small particles as a function of wavelength and temperature is presented. The temperature ranges of interest are 300 to 500 K and 1000 to 3000 K for wavelengths spanning 0.3 to 10 μm. Particulate species are pure form Al_2O_3, ZrO_2, MgO, C, and ZrC in addition to rocket exhaust derived particles; the radii for these particles will span 0.1 to 10 μm. Proposed high temperature experiments would be performed in a shock tube. A particle injector conceptual design for producing particulate dispersions over short lengths of the shock tube is presented and would be used in conjunction with the experiments. Optical response and sensitivity to index of refraction of the particulate species is investigated in detail and used to guide the optical diagnostic design. Finally, a methodology for determining the complex —

20. DISTRIBUTION/AVAILABILITY OF ABSTRACT	21. ABSTRACT SECURITY CLASSIFICATION
UNCLASSIFIED/UNLIMITED X SAME AS RPT ☐ DTIC USERS ☐	UNCLASSIFIED

22a. NAME OF RESPONSIBLE INDIVIDUAL James A. Misener, Lt, USAF	22b. TELEPHONE NUMBER (Include Area Code) (805) 277-5584	22c. OFFICE SYMBOL DYSO

DD FORM 1473, 83 APR   EDITION OF 1 JAN 73 IS OBSOLETE.   UNCLASSIFIED

SECURITY CLASSIFICATION OF THIS PAGE

Block 19:
indices of refraction based upon experimental results is presented with the
recommendations for the optical diagnostic package.

Block 11:

AND PRELIMINARY DESIGN (U)

CONTENTS

iii

FIGURES

1. INTRODUCTION

The overall goal for this project has been an experimental design for the determination of the complex indices of refraction for small particles over a wide range in temperature and wavelength. Two temperature ranges of interest exist: 300 to 500 K and 1000 to 3000 K. The wavelength range is 0.3 to 10.0 μm, and the species of interest are Al_2O_3, ZrO_2, MgO, C, and ZrC. Particle sizes will range from 0.1 to 10.0 μm in radius. The area of emphasis for the experiment is the higher temperature range (1000 to 3000 K) and the infrared wavelengths (1.0 to 10.0 μm).

The project can be segmented into three distinct tasks: 1) production of the experimental environment, 2) optical data analysis and conversion to complex indices of refraction, and 3) the optical diagnostic design. These tasks are discussed in detail in Sections 2, 3, and 4, respectively. Task 1, environment production, considers the technologies available for producing particles or particle dispersions at the required temperatures while maintaining an appropriate optical access. Task 2, data analysis and conversion, considers in detail what optical measurements are appropriate, investigates their sensitivity to the complex index of refraction, defines a methodology for inverting experimental data and identifies the errors associated with the experimental measurement and inversion process. Finally, Task 3 details the specific optical measurement system that will produce the data required by Task 2.

2. EXPERIMENTAL ENVIRONMENT PRODUCTION

The creation of an experimental environment suitable for this project is addressed by defining appropriate techniques for producing the high and low temperature environments, and by designing a system that will produce particle dispersions within this environment. Section 2.1 discusses the high temperature system, Section 2.2 presents the basic concepts for a low temperature system, and Section 2.3 presents the design for the particle delivery system.

2.1 High Temperature System

A major portion of the experimental effort is the production of a steady and definable high temperature environment for the particles. The temperature range must be 1000 to 3000 K, with good optical access to the temperature field. Previous experimental efforts have utilized laser heating, direct flame contact heating, and shock tubes. In addition, the recent development of graphite tube furnaces makes the 3000 K temperature attainable in a furnace system.

Electrostatically levitating a single particle while irradiating it with high power density Nd:YAG lasers was explored by Dowling and Randall (Ref. 1). This technique proved to be exceptionally difficult to implement due to two significant problems. The laser-particle interaction displaced the particle out of the levitating electric field. In addition, optical emission and extinction signals were small, which mandated data collection and averaging over a long time period. Subsequent work by Pluchino et al. (Ref. 2) has dropped the laser heating concept and produced room temperature refractive index data for carbon at 0.488 μm.

Particle heating by direct contact with a flame has been utilized by Mularz and Yuen (Ref. 3) and Adams (Ref. 4). Both works were concerned with temperatures between 2000 and 3000 K and used alumina as the subject specie. Several problems are inherent to this technique. The interaction of the particle with active species through the flame zone will possibly produce a

2

contaminated particle, thus adding a very hard to quantify error to the experiment. In addition, the temperature of the particles will change with their position in the flame, which implies that a temperature map for the flame would have to be produced and used to determine the particle temperatures. Mularz and Yuen (Ref. 3) also report difficulties associated with the mass loading of the flame with the subject specie as well as agglomeration within and downstream of the flame zone.

Carlson (Ref. 5) also investigated a direct flame contact approach with a H_2-O_2 rocket motor seeded with alumina and magnesium oxide. Although he was successful in quantifying the emissivity of Al_2O_3 as it changes phase, specifying the temperature field was a significant problem, and background emission from the combusting species and products significantly complicated the optical measurements.

Graphite tube furnaces provide a reasonable method of producing temperatures up to 3000 K. However, providing optical access and a stable particulate dispersion would be a major technical challenge. Optical access is difficult due to the cooling required to allow windows to survive the extreme temperatures. In addition, the background radiation due to the furnace walls would be very large. In brief, a high temperature furnace, although appearing simple in concept, would be exceptionally hard to integrate into this experiment.

High temperature measurements are commonly performed in shock tubes for a variety of experimental studies. Nettleton (Ref. 6) has done an extensive review of previous shock tube work with non-gas phase species and discusses a wealth of literature on the shock heating of particles, blast waves, explosive sensitivity, slab combustion, and detonation. Konopka et al. (Ref. 7), also described in Calia el al. (Ref. 8), applied shock tube technology to quantify the radiation from typical rocket plume particulates and reported the technique as a successful means of producing a high temperature field of particles.

In summary, high temperature experiments demand a well quantified and steady environment, and three candidates have been examined in the literature in addition to the graphite furnace technique. Laser heating single particles appears to be an exceptionally difficult experiment which would require a significant development effort. Flame-particle interaction techniques produce particles of questionable composition, thus introducing an unacceptable error. The high temperature furnace concept is complicated by the problems of optical access.

We believe a reflected zone shock-tube technique provides a simple means of heating the particles and is the most appropriate experimental technique available. In addition to the work of Konopka et al. (Ref. 7) in which they reported no difficulties with the operation of the shock tube, PSI has performed several shock-tube studies and is confident of the technique. Production of the high temperature environment will be accomplished most effectively in a shock tube.

2.1.1 **Shock Tube Basics** - Shock tubes are used to provide a transient high temperature environment; their major limitation is the time duration of the elevated temperature field. The time required for this experiment is the time necessary for temperature equilibration and subsequent optical measurements. This "working" time is dependent upon several of the parameters relevant to the shock tube's operation. In this section a development of the specific dependencies is presented along with a brief discussion of the basics of shock tube operation.

Shock tubes are typically discussed with x-t diagrams, as in Leipman and Roshko (Ref. 9) and Gaydon and Hurle (Ref. 10), which allow description of the evolution in distance and time of the shock wave, contact discontinuity, and rarefaction wave, as shown in Figure 1. Before the diaphragm breaks, at time 0, the driver section is filled with quiescent gas at pressure P_4 and temperature T_4. Similarly the test section is filled with quiescent gas at pressure P_1 and temperature T_1. When the diaphragm breaks, a shock wave propagates through the test section followed by the contact discontinuity, which is a

4
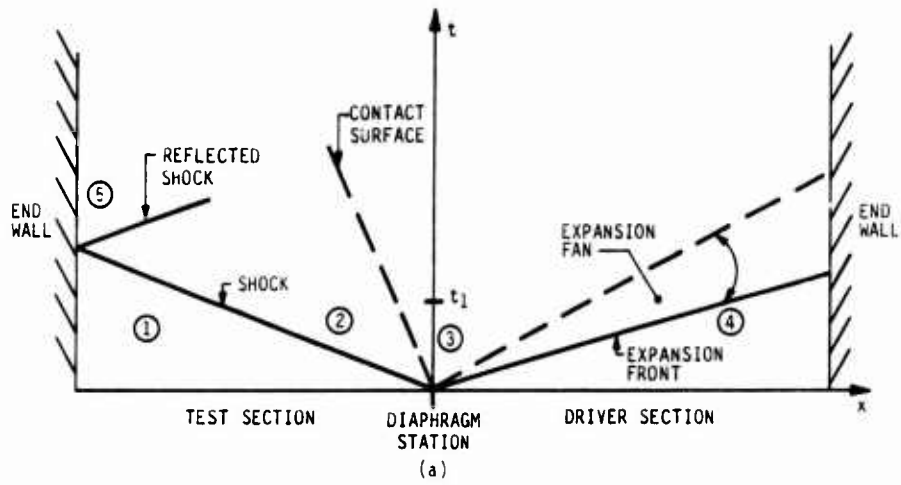
Figure 1(a). Fluid motion in a shock tube.
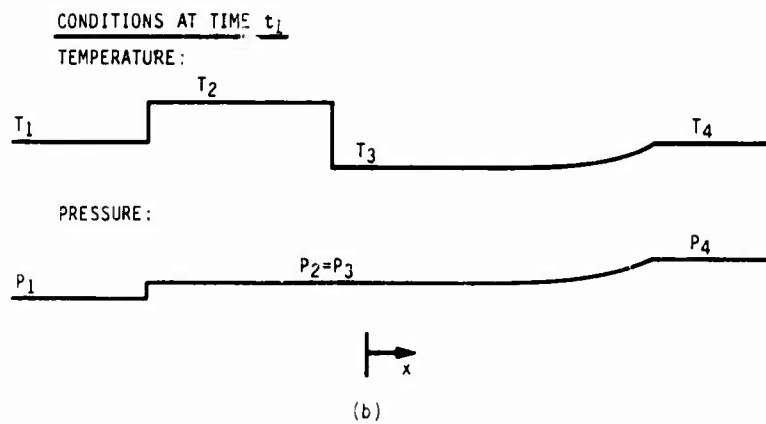
Figure 1(b). Fluid state at time t_1.

5

surface that separates the test gas and driver gas. Pressure and velocity are equal across this surface. A rarefaction front, traveling at the local speed of sound, propagates into the driver section and is followed by an expansion fan which is a field of varying temperature, pressure, and velocity that separates the quiescent gas in Region 4 from the flowing constant temperature and pressure gas in Region 3. Thus, when the diaphragm breaks, a transient flow begins. Regions 1 and 4 are the original, unaffected regions in the shock tube. Regions 2 and 3 are the flowing regions, with equal velocity. Pressures and temperatures within the shock tube at a fixed time, t_1, are shown in Figure 1(b). As previously stated, the pressures and temperatures in Regions 1 and 4 are at their original levels. Region 2 is the gas that has been heated by the shock, explaining the increased pressure and temperature. Region 3 contains the gas that has undergone an expansion, thus lowering the temperature and pressure from the starting value in Region 4.

The optical measurements for this project will take place in Region 5 which is a quiescent region through which the reflected shock has passed. The problem from an experimental design point of view is to predict the temperature, pressure and duration of Region 5 to insure that these parameters are appropriate for the experiment. The equations which describe this behavior are straightforward algebraic expressions and are derived in Gaydon and Hurle (Ref. 10). However, their form dictates iterative solutions. The two relations required to specify the pressure in the reflected shock zone, P_5, are given by Eqs. (1) and (2).

$$P_4/P_1 = P_2/P_1 \left[1 - \frac{(\gamma_D-1)(a_1/a_4)(\xi-1)}{\sqrt{2\gamma_T}\sqrt{2\gamma_T + (\gamma_T+1)(\xi-1)}} \right]^{\frac{-2\gamma_D}{\gamma_D-1}} \tag{1}$$

$$P_5/P_2 = \frac{(3\gamma_T-1)\,P_2/P_1 - (\gamma_T-1)}{(\gamma_T+1) + (\gamma_T-1)\,P_2/P_1} \tag{2}$$

Equations (3), (4), and (5) describe the temperature in Region 5.

6

$$\xi = P_2/P_1 \tag{3a}$$

$$\xi' = P_5/P_2 \tag{3b}$$

$$f(\xi) = \xi \frac{(\gamma_T - 1)\xi + (\gamma_T + 1)}{(\gamma_T + 1)\xi + (\gamma_T - 1)} \tag{4}$$

$$T_5/T_1 = f(\xi) \, f(\xi') \tag{5}$$

A full list of variables and their meanings is given in Table 1.

TABLE 1. Variables for the Shock Tube Equations.

a - speed of sound

L - length

M - Mach number

P - pressure

u - velocity

x - distance from the diaphragm station

t - time

T - temperature

γ - specific heat ratio

Subscripts

c - contact surface

D - driver section

T - test section

r - rarefaction front

1,2,3,4 - conditions shown in Figure 1

The working time in Region 5 is determined by the interaction of the reflected shock with the contact surface, provided that the driver meets a certain minimum length requirement. The shock-contact surface interaction is shown in Figure 2 along with the working time, τ_w, which is the time between wave arrivals at the end wall.

As shown in this figure, the reflected shock and contact surface meet and produce two waves: a weak reflected shock and a transmitted shock. The working time in the reflected shock zone is the sum of two intervals: the time for the reflected shock to meet the contact surface, τ_1, and the time for the shock reflected off the contact surface to strike the end wall, τ_2. The first interval τ_1 is found by equating the position of the reflected shock, Eq. (6), with that of the contact surface, Eq. (7), to find the time, t, Eq. (8). τ_1, Eq. (10), is the difference between this time and the time for the incident shock to hit the end wall.
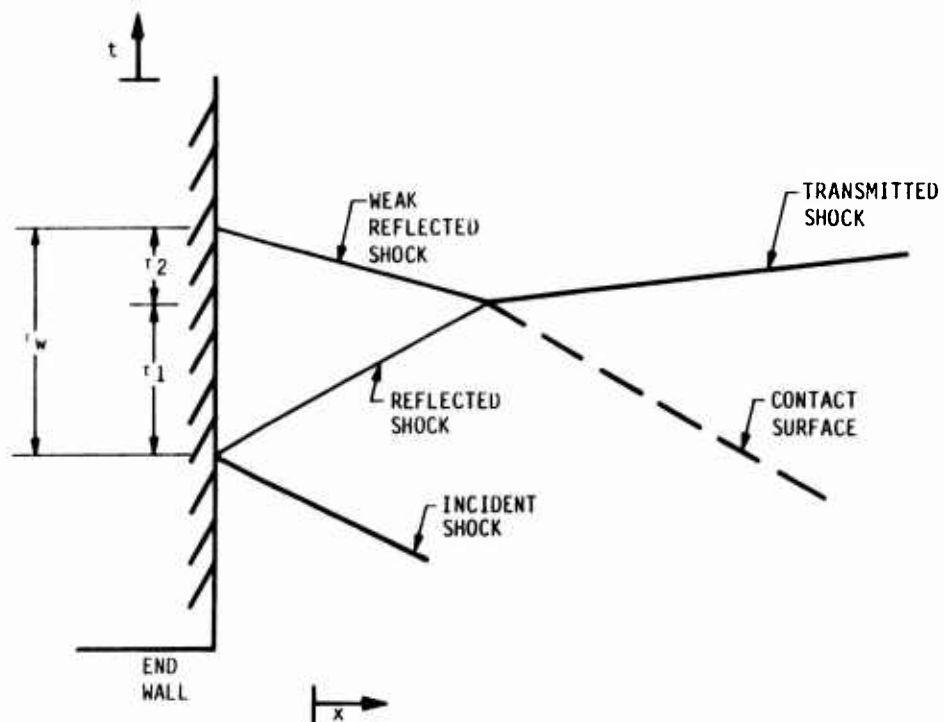
Figure 2. Interaction of the reflected shock with the contact surface.

8

$$x_c = u_3 t \qquad (6)$$

$$x_r = L_2 - (M_2 a_2 - u_2)(t_i - t') \qquad (7)$$

$$t_i = \frac{L_2 + t'\left[M_2 a_2 - u_2\right]}{M_2 a_2} \qquad (8)$$

$$t' = L_2/M_1 A_1 \qquad (9)$$

$$\tau_1 = \frac{L_2}{M_1 a_1} \left[\frac{M_1 a_1 + M_2 a_2 - u_2}{M_2 a_2}\right] \qquad (10)$$

The second interval, τ_2, is conservatively approximated by assuming the weak reflected shock to have a Mach number of 1. Therefore, τ_2 is equal to the distance traveled by the reflected shock divided by the speed of sound in the reflected shock zone, Eq. (11), and the total working time, τ_w, is the sum of τ_1 and τ_2, Eq. (12).

$$\tau_2 = \frac{\left[M_2 a_2 - u_2\right]\tau_1}{a_5} \qquad (11)$$

$$\tau_w = \tau_1 + \tau_2 \qquad (12)$$

This discussion of the working time in the reflected shock zone assumes that the reflected head of the expansion wave has not passed through the contact surface and is a reasonable assumption if the driver section is long enough. Figure 3 illustrates the evolution of the rarefaction wave for the minimum length driver section required for no rarefaction effects in the reflected shock zone during the working time, τ_w. This condition dictates that the rarefaction head meets the contact surface no sooner than the end of the period τ_1. The time at which the expansion front meets the contact surface is given by Eq. (13); the development of this equation is given in Gaydon and Hurle (Ref. 10). This time is equated to the time it takes the reflected shock to meet the contact surface, Eq. (8), which yields the required ratio of driver length to test length, Eq. (14).

9
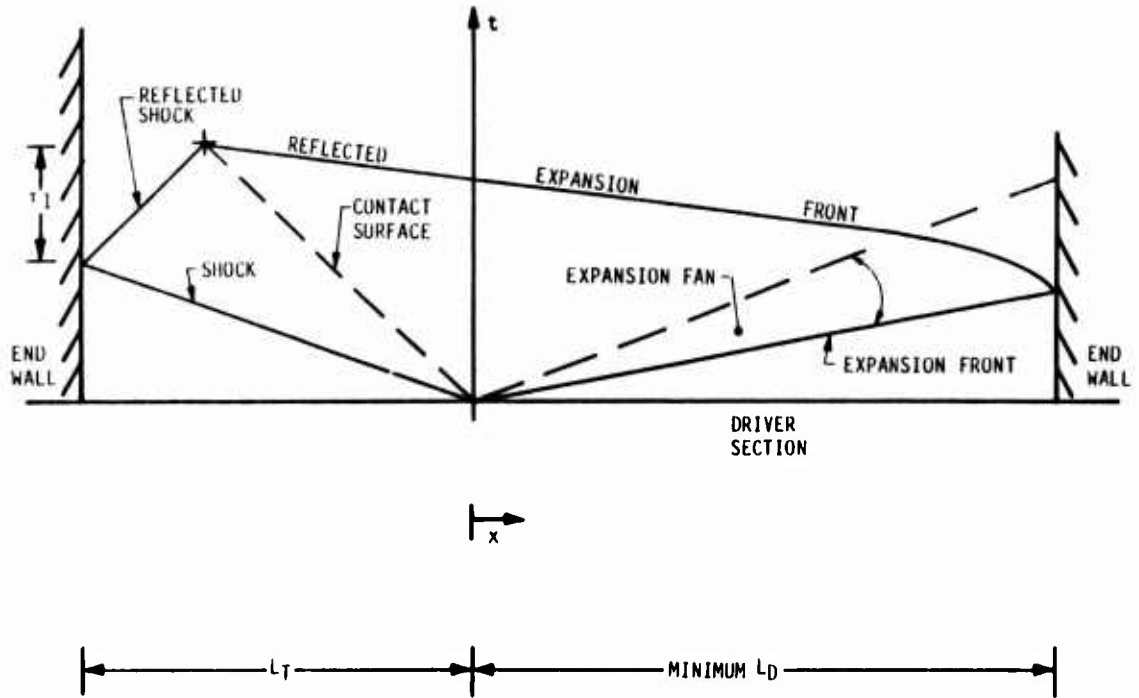
Figure 3. **Rarefaction wave interaction with the contact surface.**

$$t_i = \frac{2L_D}{a_4}\left(1 + \frac{\gamma_D - 1}{2}M_3\right)^{\frac{\gamma_D + 1}{2(\gamma_D + 1)}}$$ (13)

$$L_D/L_T = \frac{[M_1 a_1 + M_2 a_2 - u_2]}{M_1 a_1 \, M_2 a_2} \frac{a_4}{2}\left(1 + \frac{\gamma_D - 1}{2}M_3\right)^{-\left(\frac{\gamma_D + 1}{2(\gamma_D - 1)}\right)}$$ (14)

Given these relationships, the working time in the shock tube can be related to the test gas and the temperature in the reflected shock zone, as tabulated for hydrogen-argon, helium-argon and nitrogen-argon systems in Tables 2, 3 and 4. These tables clearly indicate that the working time decreases at the higher temperatures. The driver length-to-test length ratio, listed in the tables illustrates that the maximum driver length is required at the lower temperatures. The initial and reflected pressure ratio in the shock tube, P_4/P_1, and P_5/P_1, are also given in Tables 2, 3, and 4 as a function of temperature in the reflected shock zone.

10

TABLE 2.   Shock Conditions for a Hydrogen Argon System.

Working time, tau, is given in seconds per meter of test section.
LDLT is the minimum ratio of driver-to-test lengths.
M1 and M5 are the incident and reflected shock strengths.

```
INITIAL GAS TEMPERATURE IS    300.  K
DRIVER GAS IS HYDROGEN  , GAMMA IS    1.41, R IS   4122.0
TEST GAS IS ARGON         GAMMA IS    1.67, R IS    208.0
```

T5	TAU	LDLT	P2/P1	P4/P1	P5/P1	M1	M5
800.0	0.131E-02	1.690799	3.490	4.729	9.285	1.729	1.526
850.0	0.122E-02	1.614811	3.757	5.203	10.427	1.790	1.555
900.0	0.113E-02	1.547609	4.026	5.692	11.606	1.849	1.583
950.0	0.106E-02	1.487687	4.295	6.196	12.816	1.906	1.608
1000.0	0.995E-03	1.433874	4.565	6.714	14.055	1.962	1.631
1050.0	0.940E-03	1.385234	4.836	7.246	15.320	2.017	1.653
1100.0	0.892E-03	1.341012	5.108	7.792	16.610	2.070	1.673
1150.0	0.848E-03	1.300604	5.380	8.352	17.921	2.122	1.692
1200.0	0.810E-03	1.263505	5.652	8.925	19.252	2.172	1.710
1250.0	0.775E-03	1.229298	5.925	9.512	20.602	2.222	1.726
1300.0	0.743E-03	1.197636	6.198	10.112	21.968	2.270	1.742
1350.0	0.715E-03	1.168227	6.471	10.725	23.350	2.318	1.756
1400.0	0.688E-03	1.140823	6.745	11.352	24.745	2.365	1.770
1450.0	0.665E-03	1.115204	7.018	11.992	26.155	2.411	1.783
1500.0	0.643E-03	1.091199	7.292	12.644	27.576	2.456	1.795
1550.0	0.622E-03	1.068643	7.567	13.310	29.008	2.500	1.807
1600.0	0.603E-03	1.047397	7.841	13.989	30.452	2.543	1.818
1650.0	0.586E-03	1.027347	8.115	14.680	31.904	2.586	1.828
1700.0	0.570E-03	1.008379	8.390	15.385	33.367	2.628	1.838
1750.0	0.555E-03	0.990405	8.665	16.103	34.837	2.670	1.848
1800.0	0.540E-03	0.973341	8.940	16.834	36.316	2.711	1.857
1850.0	0.527E-03	0.957118	9.215	17.577	37.802	2.751	1.865
1900.0	0.515E-03	0.941666	9.490	18.334	39.295	2.790	1.874
1950.0	0.503E-03	0.926924	9.765	19.104	40.795	2.830	1.882
2000.0	0.492E-03	0.912848	10.040	19.886	42.300	2.868	1.889
2050.0	0.481E-03	0.899379	10.315	20.682	43.812	2.906	1.896
2100.0	0.471E-03	0.886489	10.591	21.491	45.329	2.944	1.903
2150.0	0.462E-03	0.874124	10.866	22.313	46.852	2.981	1.910
2200.0	0.453E-03	0.862260	11.142	23.148	48.379	3.018	1.916
2250.0	0.444E-03	0.850858	11.417	23.996	49.911	3.054	1.922
2300.0	0.436E-03	0.839893	11.693	24.857	51.447	3.090	1.928
2350.0	0.429E-03	0.829336	11.968	25.732	52.988	3.125	1.934
2400.0	0.421E-03	0.819164	12.244	26.620	54.532	3.160	1.939
2450.0	0.414E-03	0.809352	12.520	27.521	56.080	3.195	1.945
2500.0	0.407E-03	0.799882	12.795	28.435	57.632	3.229	1.950
2550.0	0.401E-03	0.790731	13.071	29.364	59.187	3.263	1.955
2600.0	0.395E-03	0.781889	13.347	30.305	60.745	3.297	1.959
2650.0	0.389E-03	0.773330	13.623	31.260	62.307	3.330	1.964
2700.0	0.383E-03	0.765047	13.899	32.228	63.871	3.363	1.968
2750.0	0.378E-03	0.757021	14.175	33.211	65.439	3.396	1.973
2800.0	0.372E-03	0.749241	14.451	34.206	67.008	3.428	1.977
2850.0	0.367E-03	0.741694	14.726	35.216	68.581	3.460	1.981
2900.0	0.362E-03	0.734368	15.002	36.239	70.156	3.492	1.985
2950.0	0.358E-03	0.727256	15.278	37.276	71.732	3.523	1.988
3000.0	0.353E-03	0.720343	15.554	38.328	73.312	3.555	1.992
3050.0	0.349E-03	0.713624	15.830	39.393	74.893	3.585	1.996
3100.0	0.345E-03	0.707085	16.107	40.472	76.477	3.616	1.999
3150.0	0.340E-03	0.700725	16.383	41.565	78.062	3.646	2.002
3200.0	0.336E-03	0.694531	16.659	42.672	79.650	3.677	2.006

TABLE 3.   Shock Conditions for a Helium Argon System.

INITIAL GAS TEMPERATURE IS   300. K
DRIVER GAS IS helium   , GAMMA IS   1.66, R IS   2075.1
TEST GAS IS argon   GAMMA IS   1.67, R IS   208.0

TS	TAU	LDLT	P2/P1	P4/P1	PS/P1	M1	MS
800.0	0.131E-02	1.301674	3.490	5.619	9.285	1.729	1.526
850.0	0.122E-02	1.243173	3.757	6.265	10.427	1.790	1.555
900.0	0.113E-02	1.191437	4.026	6.943	11.606	1.849	1.583
950.0	0.106E-02	1.145306	4.295	7.652	12.816	1.906	1.608
1000.0	0.995E-03	1.103878	4.565	8.394	14.055	1.962	1.631
1050.0	0.940E-03	1.066432	4.836	9.167	15.320	2.017	1.653
1100.0	0.892E-03	1.032387	5.108	9.972	16.610	2.070	1.673
1150.0	0.848E-03	1.001279	5.380	10.810	17.921	2.122	1.692
1200.0	0.810E-03	0.972718	5.652	11.681	19.252	2.172	1.710
1250.0	0.775E-03	0.946383	5.925	12.584	20.602	2.222	1.726
1300.0	0.743E-03	0.922008	6.198	13.522	21.968	2.270	1.742
1350.0	0.715E-03	0.899367	6.471	14.493	23.350	2.318	1.756
1400.0	0.688E-03	0.878270	6.745	15.498	24.745	2.365	1.770
1450.0	0.665E-03	0.858548	7.018	16.538	26.155	2.411	1.783
1500.0	0.643E-03	0.840067	7.292	17.614	27.576	2.456	1.795
1550.0	0.622E-03	0.822702	7.567	18.725	29.008	2.500	1.807
1600.0	0.603E-03	0.806346	7.841	19.872	30.452	2.543	1.818
1650.0	0.586E-03	0.790910	8.115	21.056	31.904	2.586	1.828
1700.0	0.570E-03	0.776307	8.390	22.277	33.367	2.628	1.838
1750.0	0.555E-03	0.762470	8.665	23.537	34.837	2.670	1.848
1800.0	0.540E-03	0.749333	8.940	24.834	36.316	2.711	1.857
1850.0	0.527E-03	0.736844	9.215	26.171	37.802	2.751	1.865
1900.0	0.515E-03	0.724948	9.490	27.547	39.295	2.790	1.874
1950.0	0.503E-03	0.713599	9.765	28.964	40.795	2.830	1.882
2000.0	0.492E-03	0.702762	10.040	30.421	42.300	2.868	1.889
2050.0	0.481E-03	0.692393	10.315	31.921	43.812	2.906	1.896
2100.0	0.471E-03	0.682469	10.591	33.462	45.329	2.944	1.903
2150.0	0.462E-03	0.672951	10.866	35.046	46.852	2.981	1.910
2200.0	0.453E-03	0.663817	11.142	36.674	48.379	3.018	1.916
2250.0	0.444E-03	0.655039	11.417	38.347	49.911	3.054	1.922
2300.0	0.436E-03	0.646597	11.693	40.064	51.447	3.090	1.928
2350.0	0.429E-03	0.638470	11.968	41.827	52.988	3.125	1.934
2400.0	0.421E-03	0.630639	12.244	43.637	54.532	3.160	1.939
2450.0	0.414E-03	0.623085	12.520	45.495	56.080	3.195	1.945
2500.0	0.407E-03	0.615794	12.795	47.400	57.632	3.229	1.950
2550.0	0.401E-03	0.608750	13.071	49.355	59.187	3.263	1.955
2600.0	0.395E-03	0.601943	13.347	51.359	60.745	3.297	1.959
2650.0	0.389E-03	0.595353	13.623	53.414	62.307	3.330	1.964
2700.0	0.383E-03	0.588977	13.899	55.520	63.871	3.363	1.968
2750.0	0.378E-03	0.582798	14.175	57.679	65.439	3.396	1.973
2800.0	0.372E-03	0.576808	14.451	59.891	67.008	3.428	1.977
2850.0	0.367E-03	0.321407	14.726	62.157	68.581	3.460	1.981
2900.0	0.362E-03	0.318232	15.002	64.479	70.156	3.492	1.985
2950.0	0.358E-03	0.315150	15.278	66.855	71.732	3.523	1.988
3000.0	0.353E-03	0.312155	15.554	69.289	73.312	3.555	1.992
3050.0	0.349E-03	0.309243	15.830	71.781	74.893	3.585	1.996
3100.0	0.345E-03	0.306409	16.107	74.333	76.477	3.616	1.999
3150.0	0.340E-03	0.303653	16.383	76.943	78.062	3.646	2.002
3200.0	0.336E-03	0.300969	16.659	79.615	79.650	3.677	2.006

TABLE 4. Shock Conditions for a Nitrogen Argon System.

```
INITIAL GAS TEMPERATURE IS   300. K
DRIVER GAS IS NITROGEN  , GAMMA IS   1.40, R IS    296.6
TEST GAS IS ARGON       GAMMA IS   1.67, R IS    208.0
```

T5	TAU	LDLT	P2/P1	P4/P1	P5/P1	M1	M5
800.0	0.131E-02	0.270073	3.490	11.603	9.285	1.729	1.526
850.0	0.122E-02	0.247952	3.757	13.697	10.427	1.790	1.555
900.0	0.113E-02	0.228723	4.026	16.045	11.606	1.849	1.583
950.0	0.106E-02	0.211859	4.295	18.667	12.816	1.906	1.608
1000.0	0.996E-03	0.196956	4.565	21.585	14.055	1.962	1.631
1050.0	0.940E-03	0.183695	4.836	24.822	15.320	2.017	1.653
1100.0	0.892E-03	0.171822	5.108	28.405	16.610	2.070	1.673
1150.0	0.848E-03	0.161133	5.380	32.359	17.921	2.122	1.692
1200.0	0.810E-03	0.151462	5.652	36.715	19.252	2.172	1.710
1250.0	0.775E-03	0.142672	5.925	41.503	20.602	2.222	1.726
1300.0	0.743E-03	0.134650	6.198	46.757	21.968	2.270	1.742
1350.0	0.715E-03	0.127303	6.471	52.512	23.350	2.318	1.756
1400.0	0.688E-03	0.120550	6.745	58.806	24.745	2.365	1.770
1450.0	0.665E-03	0.114322	7.018	65.682	26.155	2.411	1.783
1500.0	0.643E-03	0.108564	7.292	73.180	27.576	2.456	1.795
1550.0	0.622E-03	0.103225	7.567	81.350	29.008	2.500	1.807
1600.0	0.603E-03	0.098263	7.841	90.241	30.452	2.543	1.818
1650.0	0.586E-03	0.093640	8.115	99.905	31.904	2.586	1.828
1700.0	0.570E-03	0.089324	8.390	110.402	33.367	2.628	1.838
1750.0	0.555E-03	0.085287	8.665	121.791	34.837	2.670	1.848
1800.0	0.540E-03	0.081502	8.940	134.141	36.316	2.711	1.857
1850.0	0.527E-03	0.077950	9.215	147.516	37.802	2.751	1.865
1900.0	0.515E-03	0.074610	9.490	161.995	39.295	2.790	1.874
1950.0	0.503E-03	0.071463	9.765	177.660	40.795	2.830	1.882
2000.0	0.492E-03	0.068496	10.040	194.591	42.300	2.868	1.889
2050.0	0.481E-03	0.065693	10.315	212.890	43.812	2.906	1.896
2100.0	0.471E-03	0.063043	10.591	232.638	45.329	2.944	1.903
2150.0	0.462E-03	0.060534	10.866	253.959	46.852	2.981	1.910
2200.0	0.453E-03	0.058155	11.142	276.952	48.379	3.018	1.916
2250.0	0.444E-03	0.055898	11.417	301.745	49.911	3.054	1.922
2300.0	0.436E-03	0.053755	11.693	328.458	51.447	3.090	1.928
2350.0	0.429E-03	0.051716	11.968	357.239	52.988	3.125	1.934
2400.0	0.421E-03	0.049776	12.244	388.224	54.532	3.160	1.939
2450.0	0.414E-03	0.047928	12.520	421.582	56.080	3.195	1.945
2500.0	0.408E-03	0.046167	12.795	457.471	57.632	3.229	1.950
2550.0	0.401E-03	0.044486	13.071	496.083	59.187	3.263	1.955
2600.0	0.395E-03	0.042881	13.347	537.583	60.745	3.297	1.959
2650.0	0.389E-03	0.041347	13.623	582.223	62.307	3.330	1.964
2700.0	0.383E-03	0.039882	13.899	630.176	63.871	3.363	1.968
2750.0	0.378E-03	0.038479	14.175	681.711	65.439	3.396	1.973
2800.0	0.372E-03	0.037136	14.451	737.066	67.008	3.428	1.977
2850.0	0.367E-03	0.035849	14.726	796.508	68.581	3.460	1.981
2900.0	0.363E-03	0.034616	15.002	860.352	70.156	3.492	1.985
2950.0	0.358E-03	0.033433	15.279	928.862	71.732	3.523	1.988
3000.0	0.353E-03	0.032298	15.554	1002.415	73.312	3.555	1.992
3050.0	0.349E-03	0.031209	15.830	1081.347	74.893	3.585	1.996
3100.0	0.345E-03	0.030162	16.107	1166.067	76.477	3.616	1.999
3150.0	0.340E-03	0.029156	16.383	1256.924	78.062	3.646	2.002
3200.0	0.336E-03	0.028189	16.659	1354.419	79.650	3.677	2.006

13

The relationships used to assemble Tables 2, 3, and 4 provide the basic tools for designing the shock tube experiment. The next step is to define the working time required in the reflected shock zone.

2.1.2 Particle-Temperature Equilibrium - Two parameters of importance when considering the energy exchange between the particles and the heated gas in the reflected zone of the shock tube are the change in the gas temperature and the time it takes for particle-gas equilibration occur. The change in gas temperature is directly related to the mass loading of particles and the initial temperature difference between the particles and the gas. An upper bound on number densities for the experiment is provided by setting the optical depth equal to 0.1. The optical depth is defined by Bouguer's law, Eq. (15a), and is a means of quantifying the attenuation of energy in an absorbing and scattering media. Optical depth also quantifies the type of scattering for the media: optical depths less than 0.1 produce single scattering, optical depths between 0.1 and 0.3 produce double scattering, and optical depths greater than 0.3 produce multiple scattering. This upper bound on number densities is expressed in Eq. (15b) which follows directly from setting the optical depth equal to 0.1 in the relationship between optical depth, particle number density, extinction efficiency, particle radius, and the optical path length.

$$I/I_o = e^{-\tau} \tag{15a}$$

$$N_p = \frac{0.1}{\pi \, \ell \, r^2 \, Q_{ext}} \tag{15b}$$

where:

    I/I_o - ratio of attenuated to incident intensity

     τ - optical depth

     ℓ - optical path length in the attenuating media

     r - partical radius

    Q_{ext} - extinction efficiency

14

An estimate of the number density and the resulting mass loading can be made by using 1.0 as an estimate for the extinction efficiency (Q_{ext} can be as great as 4; see Figure 42), relating the resultant number density to a mass loading of the particles. This yields number densities of 3×10^3 to 3×10^7 particles/cm^3, corresponding to the radii equal to 10.0 and 0.1 μm, respectively, which imply Al_2O_3 mass loadings of 5×10^{-5} to 5×10^{-7} gm/cm^3. This mass of particles will depress the initial temperature in the reflected shock zone. A simple energy balance can be used to quantify this temperature change, as shown in Eq. (16).

$$\Delta T_g / \Delta T_p = \left(\frac{m_p}{m_g}\right)\left(\frac{c_p}{c_g}\right)$$ (16)

where:

$\Delta T_g / \Delta T_p$ - ratio of the changes in the gas temperature to the change in the particle temperature

c_p / c_g - ratio of the particle specific heat to the gaseous specific heat

m_p / m_g - ratio of the particle mass to the mass of the gas.

As an example, for extinction efficiencies equal to one with an argon test gas, a working pressure of 20 atm, and a test temperature of 2000 K, the change in gas temperature will be between 0.025 and 2.5 percent.

The time required to reach temperature equilibrium is a more immediate design factor for the shock tube experiment and has been investigated in greater detail. A lumped mass analysis will be used to model the particle temperature response; any temperature gradients within the particle will be neglected. This approximation is commonly used for systems in which the rate of heat transfer in one part of the system is much greater than that in another. For no convective heat transfer between the gas and the particle, the ratio of the gas to particle conductivity, k_g / k_p, is a reasonable measure of the accuracy of this statement. In all cases this conductivity ratio will

15

be less than 0.1, thus justifying the assumption. An energy balance for the system is given by Eq. (17). A simplifying assumption, used for direct solution, is to consider the overall system to be one particle surrounded by a fluid at the final equilibrium temperature, T_e. This assumption allows direct integration of Eq. (17) by ignoring the variability in the gas temperature. The error that is introduced will be small and will cause an overestimation of the time to reach equilibrium, thus providing a slightly conservative estimate. Equation (18) is the integrated form of the energy balance.

$$\rho c V \frac{\partial T_p}{\partial t} = - hA(T_p - T_e) \tag{17}$$

$$\theta = \exp\left(- \frac{hAt}{\rho cV}\right) \tag{18}$$

where:

$\theta = (T_p - T_e)/(T_0 - T_e)$

T_p - particle temperature

T_e - equilibrium temperature of particle and gas

T_0 - initial particle temperature

h - convective heat transfer coefficient

A - particle surface area

ρ - particle density

c - specific heat of particle

V - particle volume

The integration for Eq. (17) assumed a constant specific heat for the particle. This approximation is appropriate provided the value which is actually used is chosen to give a conservative value for the equilibration time. A final approximation is required for a usable solution; the convective heat transfer coefficient, h, is not specified but may be approximated by quick consideration of the fluid mechanical aspects of the problem. The relative velocity between the gas and the particle will be very small. This

implies that conduction is the primary mode of heat transport, which gives h
as the ratio of gas conductivity to particle radius. If temperature equilib-
rium is defined as less than two percent difference in the particle and air
temperature, the equilibration time is given by Eq. (19):

$$\tau = \frac{4 \rho c \, r^2}{3k} \qquad (19)$$

where:

   r - particle radius
   k - gas thermal conductivity

Figure 4 displays this equilibration time versus particle radius at 1000
and 3000 K for Al_2O_3; the smaller times for 3000 K are due to the increase in
thermal conductivity of the gas. Large radius particles take a significant
time to come to temperature equilibrium, and a means of decreasing this time
is necessary. A very direct method of decreasing this time is to change the
thermal conductivity of the gas by increasing the pressure in the reflected
zone of the shock tube. This pressure could easily be driven up to 20 atm
which would increase the thermal conductivity by a factor of 20. The result-
ing equilibration times are also shown in Figure 4, and are within the working
times for reasonable length shock tubes.

Figure 4 also displays the available time for particle equilibration in
the PSI 4-in. shock tube facility. The test section is 7.2 meters long which
results in the working times shown. The driver section is 4 meters in length
which yields a driver to test length ratio of 0.56. Tables 2, 3, and 4 can be
used to determine the appropriate driving gas for the temperature in the
reflected shock zone. The lightest driving gas which produces no unwanted
rarefaction effects in the reflected shock zone is used whenever possible be-
cause of the lower operating pressures associated with the lighter gas. Argon
is used as the test section gas because of its chemically and optically inert
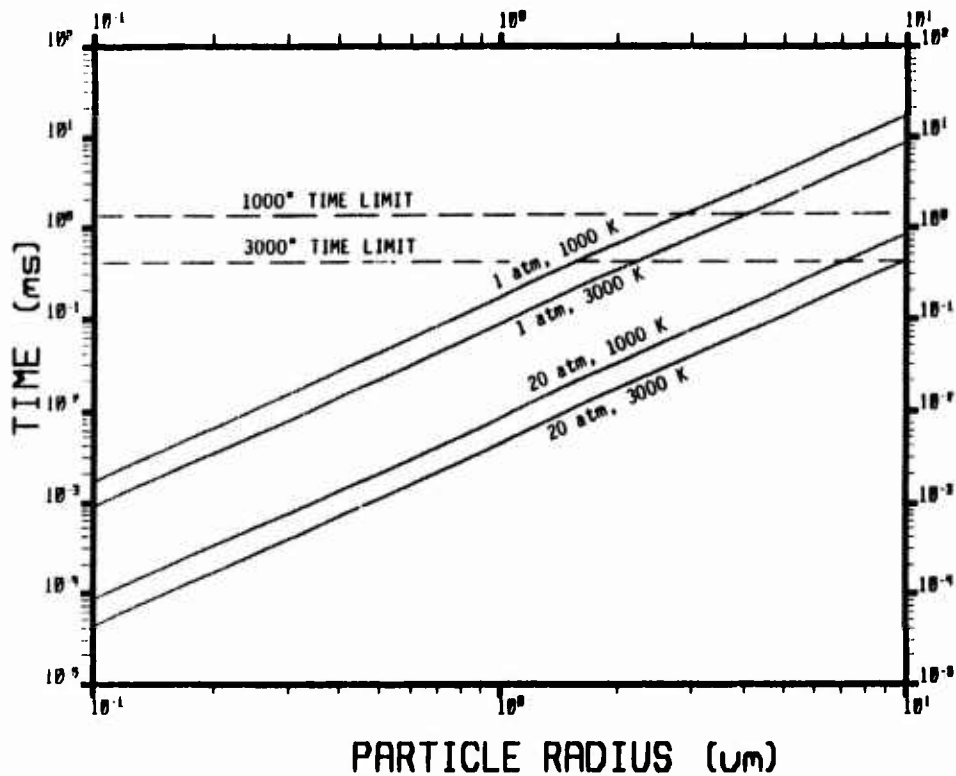
17

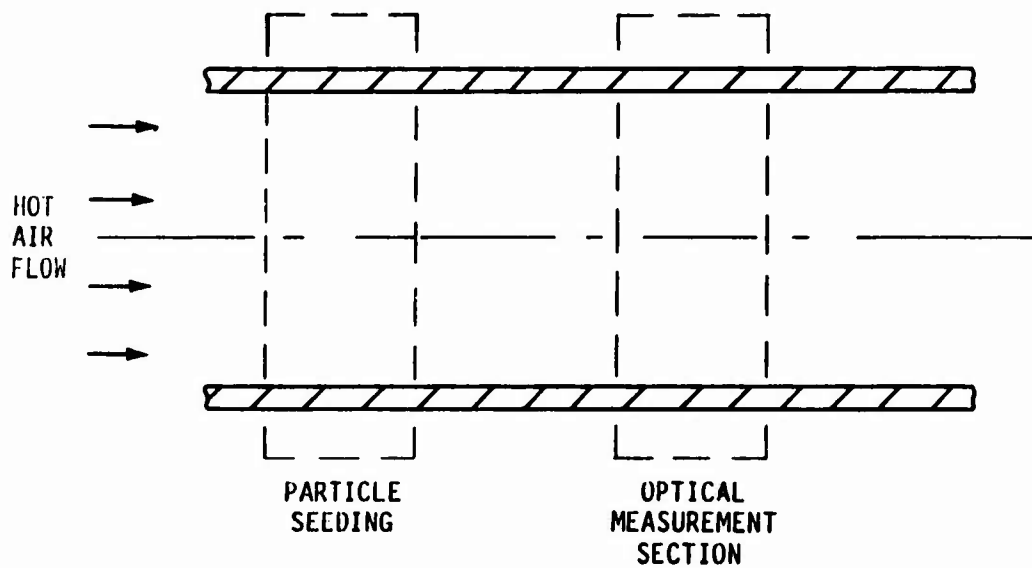Figure 4. Equilibration times for particles in the reflected shock environment.

Figure 5. Low temperature experiment concept.

behavior. Table 5 lists operating temperatures between 1000 to 3000 K along with the working time available and the shock tube gases to use.

2.2 Low Temperature Environment Concept

A conceptual design was produced for the low temperature measurements in this study. This hardware can be configured similar to a shock tube so that particle delivery hardware and optical diagnostics developed for the shock tube experiment can be readily adapted to the low temperature setup. A tubular flowing furnace system is envisioned, as shown in Figure 5. The particle seeding section is positioned upstream of the optical measurement section. Particles will remain entrained in the flow due to their small terminal velocities. These velocities may be computed from a Stokes Drag formulation and the results are presented in Figure 6.

Low terminal velocities are very accommodating since they imply that once established a dispersion of particles will be relatively stable. The low temperature experiment will be temperature-limited by the infrared background emission attributable to the furnace system and by material interaction problems between furnace and the optical access windows. This temperature limit will probably be between 600 and 800 K.

TABLE 5. Shock Tube Summary.

4-in. I.D. Tube
Test Section - 7.2m
Driver Section - 4m

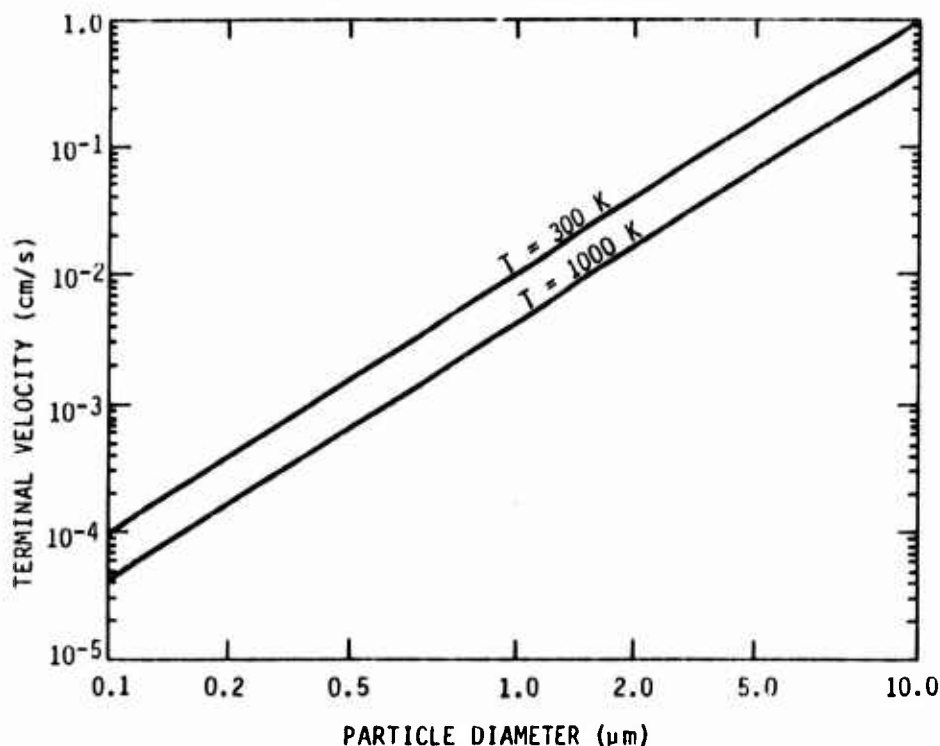| Temperature	Working Time (ms)	Gases-Driver/ Test
1000	7.2	Nitrogen/Argon
1500	4.6	Nitrogen/Argon
2000	3.5	Helium/Argon
2500	2.9	Helium/Argon
3000	2.5	Hydrogen/Argon

Figure 6. **Terminal velocity of Al$_2$O$_3$ particles in argon as a function of diameter.**

2.3 Particle Delivery System

The dispersal of the particles within the shock tube test section is an important part of the experimental design for this work. It is by no means a new problem and previous investigators have arrived at several different hardware solutions for the task. These solutions include: blowing the particles off a suspending plate in a shock tube, Calia et al. (Ref. 8); a variety of stirred or fluidized bed systems, Cann et al. (Ref. 11), and Lanzo (Ref. 12); an ultrasonic levitating system, Harris et al. (Ref. 13); an electrostatic levitating system, Adamo et al. (Ref. 14); air jet delivery systems, Decker et al. (Ref. 15); and Lowenstein and von Rosenberg (Ref. 16). Each of these solutions has its own set of operating peculiarities; the delivery system for this work is based upon the operating principles of these previously designed systems and the specialized needs of the shock tube experiment. Specific considerations which guided the particle delivery system design are: 1) production of a uniform distribution of particles in the viewing area for optical

diagnostics, 2) separation of shock tube and particle delivery system opera-
tion to allow the delivery system development to proceed independently of the
shock tube, 3) a system design which was fully cognizant of the possibility of
particle agglomeration and incorporated previous workers' empirical experience
to prevent as much agglomeration as possible, 4) the system should be easy to
use from a particle handling standpoint, and, finally, 5) the total mass of
particles required for one experiment should be substantially less than
one gram. These considerations arise from a detailed examination of the envi-
ronmental portion of the experimental design. The specific solutions to these
considerations will be discussed in conjunction with the final particle
delivery system design.

A radial particle injection system is the heart of the particle delivery
system. This concept is unique and properly capitalizes on shock tube geome-
try to produce a uniform particle distribution over a small portion of the
shock tube test section length. In contrast, axial delivery systems will
produce a cloud of particles that is unconstrained in length and diameter.
For example, a particle jet located in the end plate of the test section will
produce a relatively long cloud of particles. This cloud will follow the
spreading of the jet, which forms an approximately 10° half-angle cone accord-
ing to Pai (Ref. 17). Figure 7 illustrates this type of delivery system. The
path length through the particulate cloud varies with the diametrical path
chosen and becomes smaller close to the end plate. In addition, the uncon-
strained length of the particulate cloud would dictate larger sample loadings
for the delivery system. These considerations point to a radial injector
which delivers particles over a small axial length and produces a uniform dis-
tribution which totally fills the circular cross section of the tube.

The radial injection concept relies on an appropriate jet duration to
produce an even particle distribution. Jet duration is conveniently described
in terms of penetration depth, as done by Cetagen et al. (Ref. 18) in his
plasma jet work. The concept is depicted in Figure 8. The penetration depth,
L^*, is defined as the ratio of the volume of gas delivered to the test section
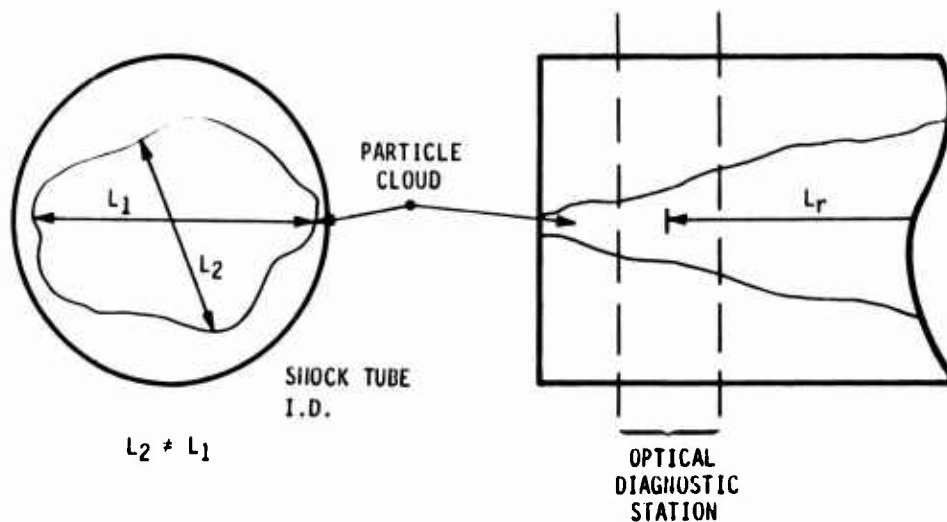to the orifice area of the jet. Under-penetration, as shown in Figure 8(a),

Figure 7. **Typical particle cloud boundaries for axial particle delivery systems.**
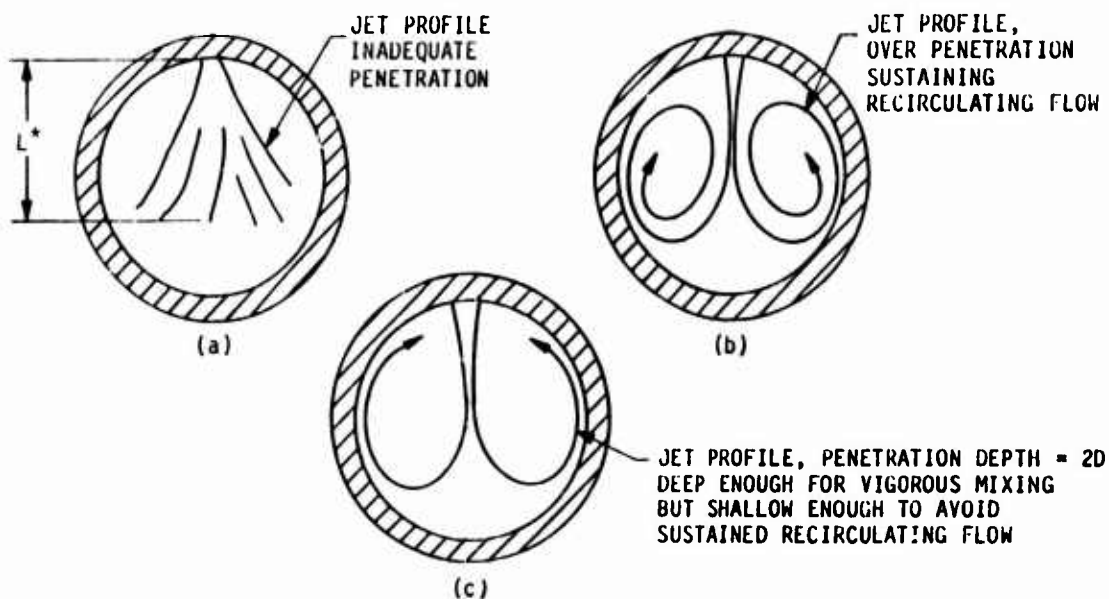
RADIAL INJECTION
$L^* = V/A_{orifice}$

Figure 8. **Penetration depth for radial injectors.**

produces an inadequate amount of mixing in the test volume. Over penetration, shown in Figure 8(b), produces a steady jet with sustained vortices. Although the mixing produced by this system is very desirable, the sustained vortices could produce an unacceptable amount of size sorting. The solution, shown in Figure 8(c), is a penetration depth greater than tube diameter but not great enough to create a steady jet flow. This optimal penetration depth will promote mixing due to the jet interaction with the wall. Optimal penetration will be determined empirically and will be on the order in a few tube diameters.

Two relevant criteria for the proper radial injector performance are that the particles remain entrained in the gas flow and that a minimal amount of size sorting occurs. The entrainment criterion is satisfied as long as the local gas stream velocity is greater than the particle terminal velocity. Size sorting can be quantified by considering particle motion in a circular path similar to that experienced when the flow changes direction at the tube wall. The forces acting on the particle are the Stokes drag, due to relative motion of the fluid, and the force from acceleration due to the circular motion. This balance of forces dictates the relationship between radial and tangential velocity given by Eq. (20).

$$v_r = \frac{2}{9} \frac{\rho_p a^2 v_t^2}{r^* \mu} \tag{20}$$

where:

v_r - radial velocity

ρ_p - particle density

a - particle radius

v_t - tangential velocity

r^* - turning radius of the flow

μ - gas viscosity

Given this relationship between velocities, size sorting can be quantified. The radial displacement of a particle, as depicted in Figure 9 along with a simplified vortex for the flow, over the flow length πr^* is given by Eq. (21).

$$\Delta = \frac{\delta}{2r^*} \frac{\pi}{9} \frac{\rho_p a^2 v_t}{\mu r^*} \tag{21}$$

where

Δ - normalized radial particle movement

δ - radial particle movement

Figure 10 illustrates the operating region for the radial injector. Local gas velocities should always be greater than the particle terminal velocity, i.e., to the right of the terminal velocity curve. To avoid size sorting in the first vortex, the gas velocity of the vortex should be less than that for Δ = 10 percent, which leaves a significant acceptable operating range for the local gas velocity of the first vortex. This size sorting analysis assumed a steady, well established flow. The jet injection system is actually a transient flow and the flow reversal vortex will not be well established, which implies that the size sorting analysis will overpredict size sorting for the system. In addition, the most severe case of size sorting has been examined; the jet is three-dimensional in nature and the vortex examined is the most severe one that will be encountered. Therefore, suitable operating velocities for the vortex may be as large as those given by the Δ = 10 percent curve. For a particle 10 μm in radius this implies a velocity in the vortex of approximately 30 cm/s. Given a jet orifice size and Eq. (22) from Pai (Ref. 17) which relates the centerline velocity of the jet at a given axial position to the exit velocity, the operating parameters for the jet may be determined. They are listed in Table 6.
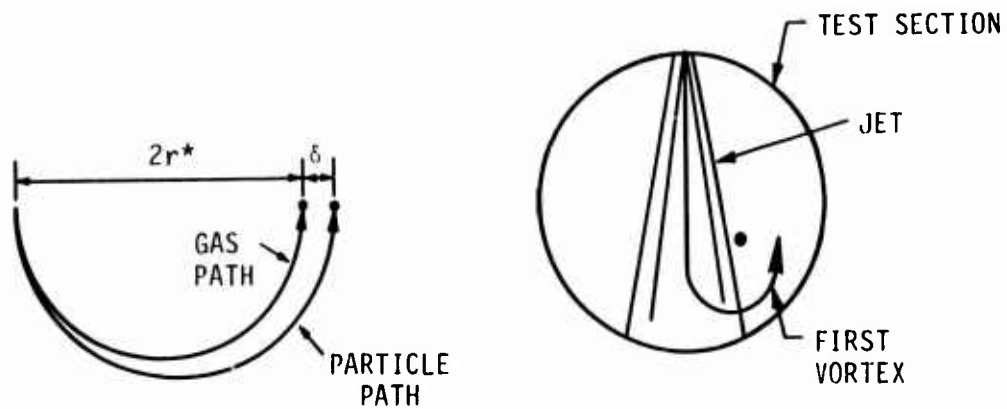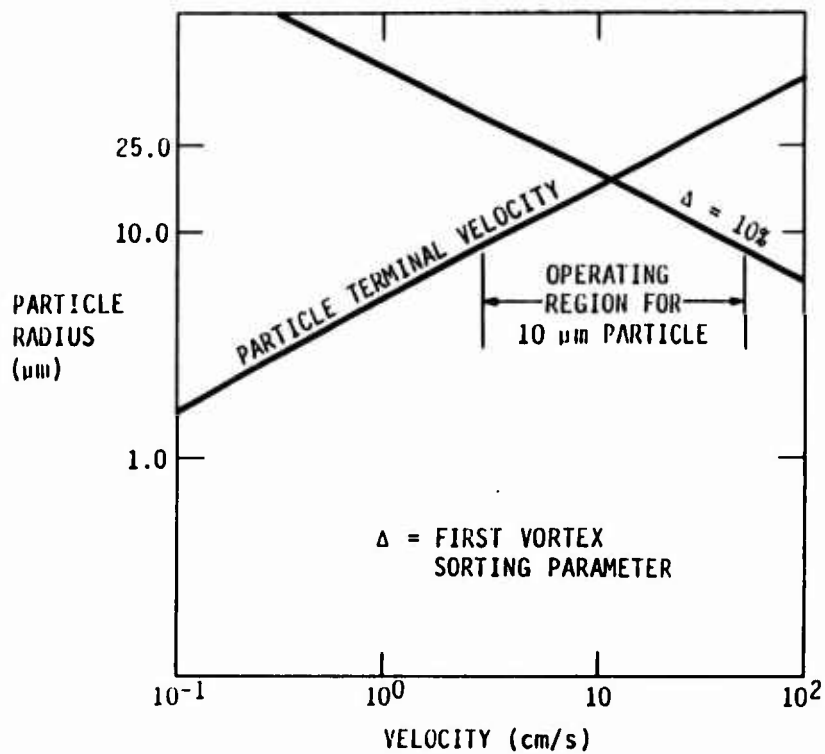
Figure 9. Relative particle motion within a vortex.

Figure 10. Operating map for radial injector, calculation of Λ assumes $\rho_p = 4$ gm/cm^3, $\mu = 2.3 \times 10^{-4}$ gm/cm^{-5}, and r* = 2 cm.

25

TABLE 6. Operating Parameters for the Radial Injection System.

Jet Exit Velocity	— 82.5 cm/s
Jet Velocity of Vortex Midpoint	— 33 cm/s
Jet Orifice Diameter	— 0.6 cm
Penetration Depth	— 30 cm (3 tube diameters)
Delivery Volume	— 8.5 cm^3
Approximate Delivery Time	— 0.36 s

$$\frac{u_c}{u_e} = 6.5 \, \frac{d'}{x} \tag{22}$$

where:

  u_c – centerline velocity of jet

  u_e – velocity of jet orifice

  d' – orifice diameter

  x – axial distance from the orifice

The integration of the radial injector to the shock tube experiment is a matter of timing; the experimental events must be sequenced so that the incident shock arrives at the optical test section after completion of particle delivery. This sequencing will not be difficult because of the relative stability of the particle dispersion once it is established. The stability is directly attributable to the low particle terminal velocities; an example is a 10 μm diameter particle of Al_2O_3. It will settle one centimeter in 1.0s when suspended in Argon at atmospheric pressure and room temperature. Therefore, the shock would have to arrive at the particle dispersion within 200 ms of the dispersal becoming stable and stagnant.

26

The proposed particle delivery system may be operated independently of the shock tube, thus reducing the set up time for each injector firing. In addition to this reducion of time between injector firings during development, the added benefit of complete optical access is accomplished by firing the injector into a plexiglass mock-up of the shock tube. The evolution of the particle dispersal can therefore be monitored and the results used to fine-tune the operation of the injector.

The particle delivery system has been defined in terms of the character-istics of a radial jet and the use of this jet within a shock tube. The hard-ware which produces the jet can now be defined. A conceptual drawing of the radial injector is shown in Figure 11. The design is very simple in concept. The piston is driven into the delivery volume producing a gas jet at the ori-fice exit. Particles are entrained in an annular volume centered on the orifice tube and through which 50 percent of the flow passes. This annular
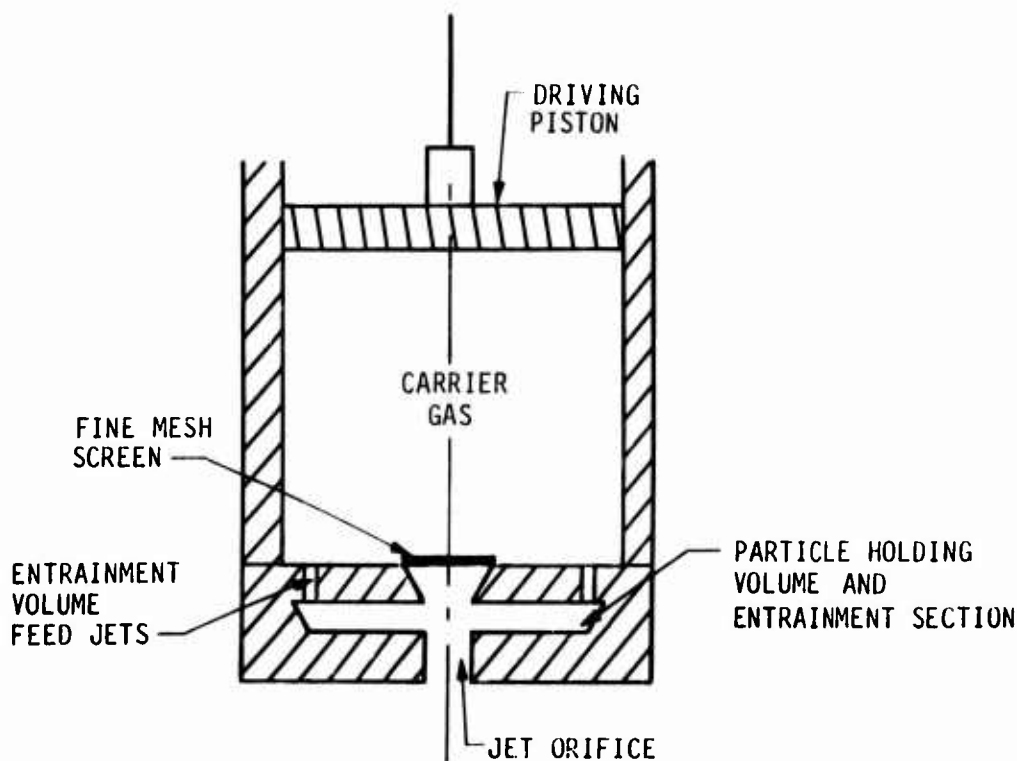

Figure 11. Cross section of the particle injector.

TABLE 7. Radial Injector Specifications.

Displacement Volume (25-mm bore, nominal stroke 17 mm, adjustable for variable displacement volume)	$8.5 \ cm^3$
Orifice Outlet Diameter	6 mm
Annular Volume (for particles to be injected)	maximum $0.5 \ cm^3$
Annulus Dimensions:	
Internal Diameter	6 mm
Outside Diameters	
Full Depth	17 mm
Zero Depth	19 mm
Orifice Feed Jet	7.25 mm diameter screened with #200 mesh. Flow Area - $14 \ mm^2$
Annulus Feed Jets	80 equally spaced on a 17.5-mm diameter circle, 0.5-mm diameter jets. Total Flow Area - $15.7 \ mm^2$
Total Jet Inlet Flow Area	$29.7 \ mm^2$
Total Jet Outlet Flow Area (6-mm diameter orifice)	$28.3 \ mm^2$
Approximate Flow Volumes Through the Annulus	10

volume can accommodate a wide range of particle loadings and, if necessary, could be modified for exceptionally high mass loadings. The flow enters the annular volume through 80 equally spaced 0.5-mm holes. To facilitate circumferential flow spreading, the jets will impinge upon a ramp in the annulus. Nominal sizes for the injector are given in Table 7.

The piston will be driven with an off-the-shelf pneumatic actuator. Flow and pressure to this linear air motor will control injection times and hold the jet piston in place during each shock event.

The radial injector will mount on the top of the shock tube; the annulus will be loaded by partially disassembling the injector. Particle volumes required for the experiments are dependent upon the optical properties of the particles and the volume into which they are delivered. Based on the angular spread of the jet, the delivery volume will be approximately 1000 cm^3 (1.5 tube diameters). The optical depth of the particle dispersion should be approximately 0.1. This value ensures that extinction and emission measurements are linearly dependent on the response of each particle in the field of view. Optical depths significantly less than 0.1 will result in an overall decreased signal level; greater optical depths produce a nonlinearity in the optical response due to multiple scattering and coincidence effects. This optical depth requirement determines the number density as previously specified by Eq. (15). The particle volumes required range from 8×10^{-4} cm^3 for 0.1 μm radii particles to 0.02 cm^3 for 10.0 μm radii particle (0.0032 gm to 0.16 gm assuming 4 gm/cm^3). This range can clearly be accommodated in the annulus.

The formation of particle agglomerates must be discouraged by the particle handling procedure and the delivery characteristics of the injector. The approach is to take all the necessary steps to produce an agglomerate free distribution. Previous workers' experience, Longacre (Ref. 19), has shown that water significantly increases the tendency to agglomerate. To combat this effect all samples will be dried before they are loaded into the injector. Prior to filling the test section, the test section and injector will be evacuated. The particles will therefore be exposed to a vacuum, and the injector heated to remove any remaining moisture. The delivery system is configured to provide a turbulent environment, due to the orifice screen and the overall turbulent nature of the jet. This will further serve to reduce agglomeration. Finally, the particle dispersal will be subjected to the incident and reflected shock which will also break up agglomerates.

In summary, the particle injector unit is simple, both in concept and in terms of hardware requirements. It addresses all of the relevant constraints for this experiment. The design is based upon the experience of other workers

who have prouuced dispersals of small particulates and the design is an adaptation of their experience to the specialized needs of this experiment. The injector can be developed independently of the experimental shock tube sequence, it capitalizes on shock tube geometry to produce a uniform particle distribution; it requires low mass loadings; and it permits significant precautions to eliminate agglomeration.

3. OPTICAL DATA ANALYSIS

Mie scattering theory defines the radiation interaction with particles in terms of the complex index of refraction of the material. This formalization of the scattering, absorption, and emission process is well documented by both van de Hulst (Ref. 20) and Kerker (Ref. 21), and the mathematics which describe this interaction are contained in a computer program written by Dave (Ref. 22). The Mie scattering computations provide the basic ingredients for this experiment. A detailed test of the Mie scattering code was performed by comparing results of Wyatt and Stull (Ref. 23). The agreement in predicted cross sections was excellent; all results were equal to the first three significant digits. In addition, the predicted radiation intensity as a function of angle was verified graphically with the results in the above reference. We feel that this code verification is exceptionally important since both the optical design and index of refraction determination are dependent upon the code.

Estimated index of refraction data is required to predict the optical response of the particulate dispersion. The complex index of refraction is a function of wavelength and temperature. Particle size does not influence the refractive index. Although the available data is sketchy for rocket exhaust particulates, a reasonable guess is provided by the following references: Adams (Ref. 14), Friese (Ref. 24), Dalzell and Sarofim (Ref. 25), Lee and Tien (Ref. 26), Ludwig et al. (Ref. 27), Whitson (Ref. 28), Mularz (Ref. 3), and Pluchino et al. (Ref. 2). Figure 12 illustrates the index of refraction data available from these references for Al_2O_3 as a function of temperature and wavelength. In several cases only one part of the two refractive indices (n,k) is available, and data from different sources are not entirely consistent. A similar amount of information is available for carbon; a very limited amount of data is available for MgO and ZrO_2, and no data has been found for ZrC. The available data has been used to construct several data sets which were then used to predict the optical response of particulate dispersions. A typical set of index of refraction curves is given for Al_2O_3 at 1000 K in Figures 13 and 14.
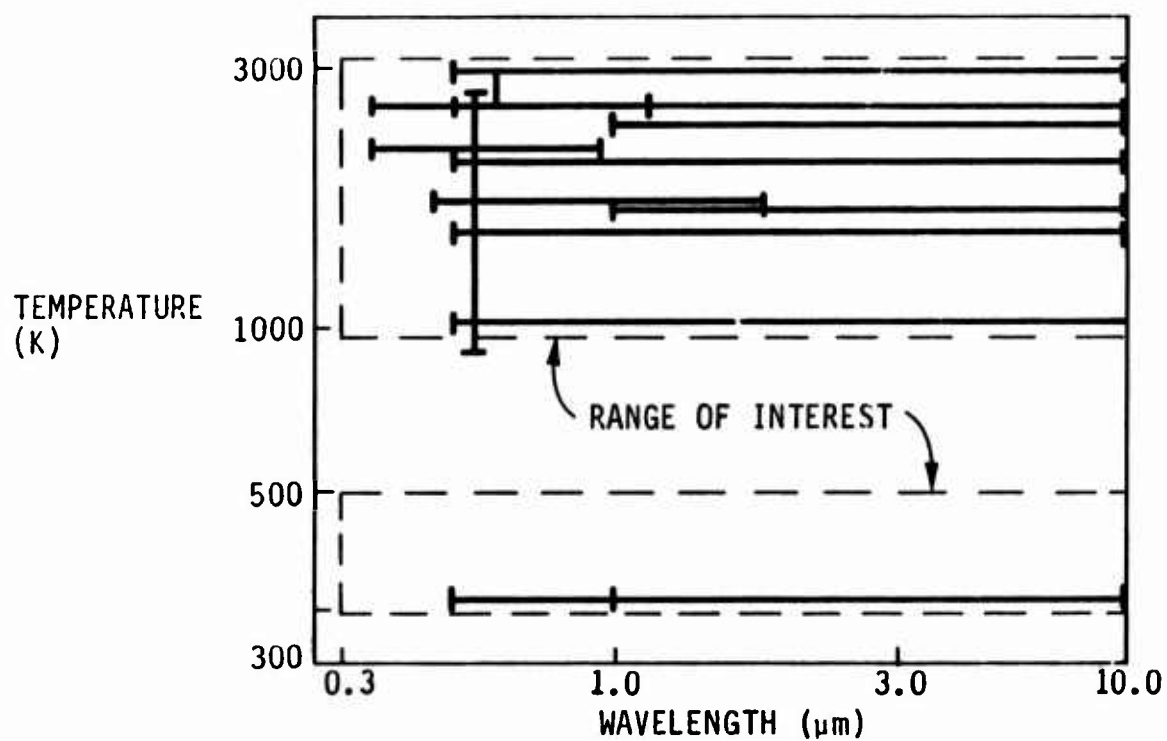
31

Figure 12. Al_2O_3 refractive index data availability.

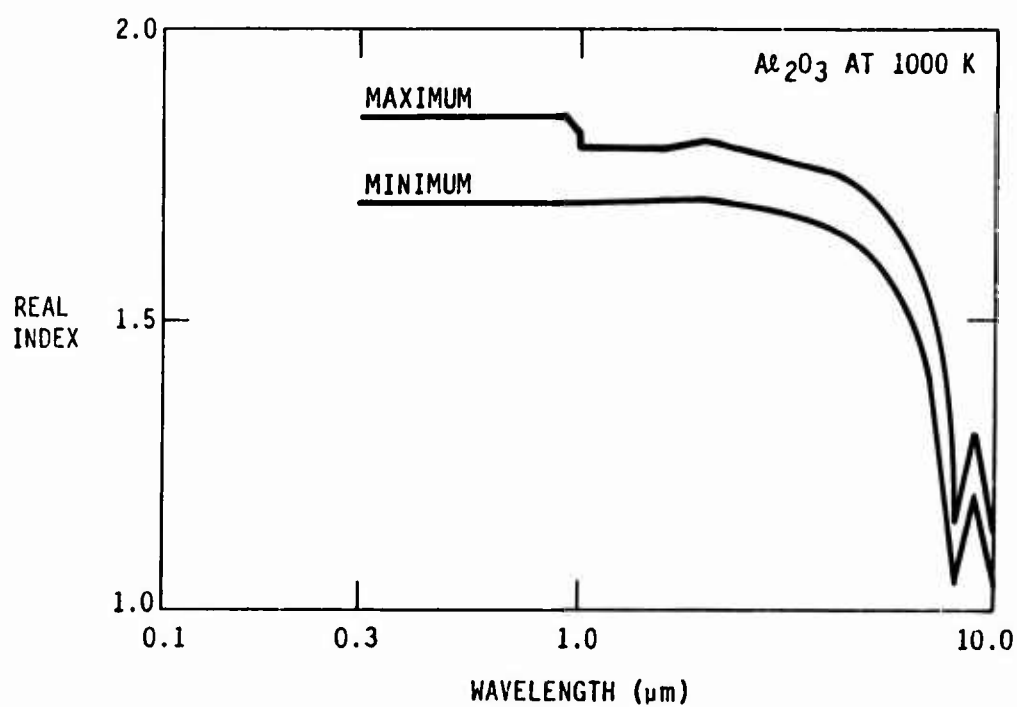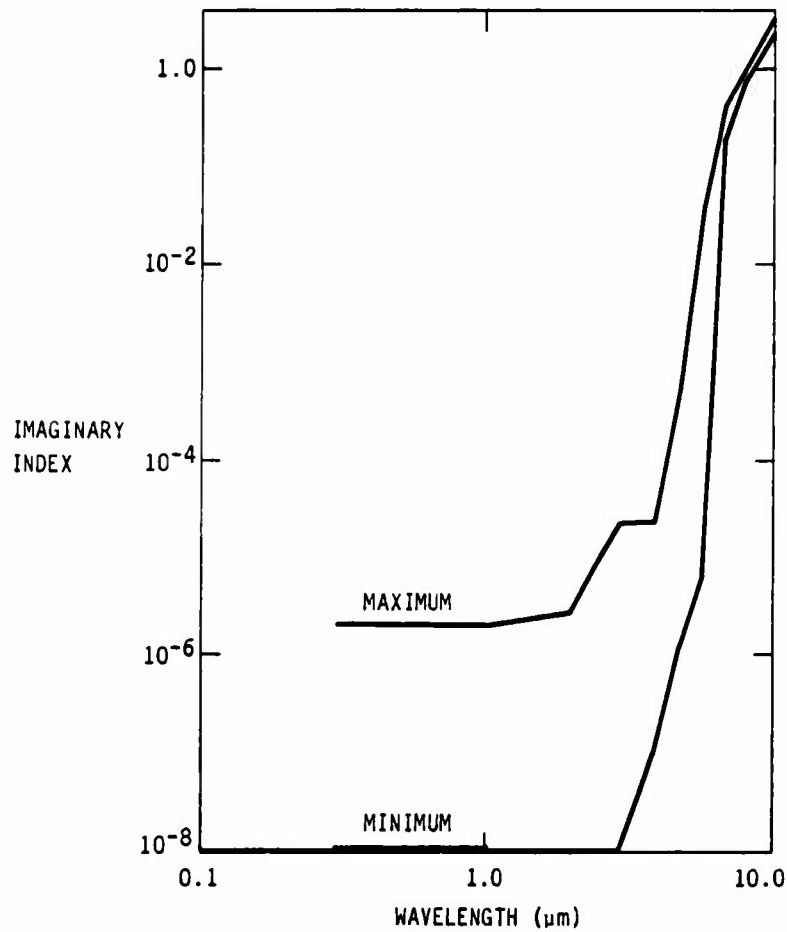Figure 13. Real index of refraction range for Al_2O_3 of 1000 K.

Figure 14. Imaginary index of refraction range for Al_2O_3 of 1000 K.

Mie scattering theory is used to predict the optical response of a particle or set of particles given the index of refraction, particle size, and radiation wavelength. Particle size and radiation wavelength are combined into one quantity, the size parameter. Given these two inputs, refractive index and size parameter, the optical response of a single particle is given. This response is represented by the extinction efficiency, Q_e, the absorption efficiency, Q_a, and the angular scattering distribution of radiation for the two polarization states. The extinction of radiation through a particulate dispersion is dependent on extinction efficiency, the number density of particles, and the optical path length, as given by the Beer-Lambert Law formalism in Eq. (23). This equation assumes all particles to be the same size; if a

33

size distribution is present, the exponential operand is replaced with an integral which represents the size distribution, Eq. (24).

$$\frac{I}{I_o} = \exp(-Q_e \ N \ \pi a^2 \ell) \tag{23}$$

where

I - observed radiation intensity

I_o - radiation intensity when no extinction occurs

Q_e - extinction efficiency

N - number density of particles

a - particle radius

ℓ - optical path length.

$$\frac{I}{I_o} = \exp \left(\int_0^\infty - Q_e(a) \ N'(a) \ \pi a^2 \ell \ da \right) \tag{24}$$

where N'(a) represents the size distribution of particles: $N = \int_0^\infty N'(a) \ da$. The effects of a size distribution will be discussed later in this section; until then a monodisperse system will be assumed.

The absorption efficiency, Q_a, is directly related to the emission from the particle dispersion. Kirchoff's law states that the spectral absorptivity is equal to the spectral emissivity. Therefore, the spectral emissivity can be determined from the absorption efficiency, as given by Eq. (25).

$$\varepsilon_\lambda = 1 - \exp(-N\pi a^2 \ Q_a \ \ell) \tag{25}$$

where

ε_λ - spectral emissivity

Q_a - absorption efficiency

Scattering is also predicted by Mie theory. This prediction takes the form of an angular light distribution for the two perpendicular polarization components of light. This implies that relating a scattered light measurement

to the results of a Mie theory calculation is potentially more difficult. Extinction and emission measurements, related to Mie theory calculations by Q_e and Q_a, are independent of polarization state and angular position. Scattering measurements are dependent on polarization and angle; therefore a scattering-based measurement is potentially more difficult to use for comparing measurements to calculation results.

The three basic measurement types—extinction, emission, and scattering—can be compared with the results of Mie theory calculations and have been introduced. In the remaining portion of this section, a method for inferring the complex index of refraction from the results of these measurements will be developed.

3.1 Sensitivity of Optical Measurements to the Index of Refraction

The overall goal for this project is to produce an experimental program that will provide as direct a measure as possible of the indices of refraction for small particles. The next step in this development is to fully understand the sensitivity of the optical measurements to the indices of refraction.

3.1.1 <u>Extinction and Emission Measurements</u> - A range of emission and extinction responses is given in Figures 15 and 16. These curves were generated based on the indices of refraction shown in Figures 13 and 14. The absorption efficiency reflects the large range of possible imaginary indices having a large range of possible values. The extinction efficiency, which includes scattering effects, has a much smaller response range, indicative of the smaller range in the real index. When examining the sensitivity of optical response to the index of refraction, remember that there are two variables that determine the optical response: size parameter and complex index of refraction. The size parameter can influence the optical response to a very large degree. A mapping of the size parameter as a function of particle radius and wavelength, shown in Figure 17, graphically illustrates that the range of possible size parameters is from 0.1 to 100. As an input to the Mie
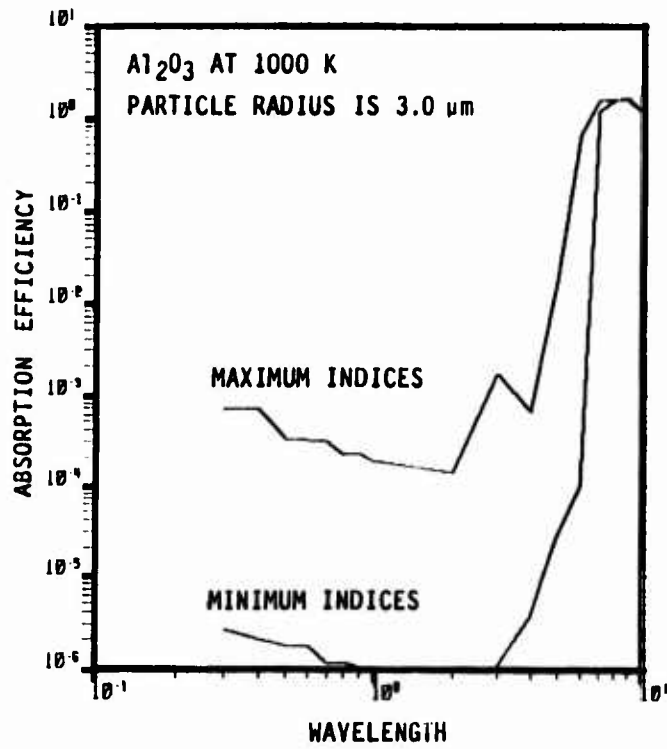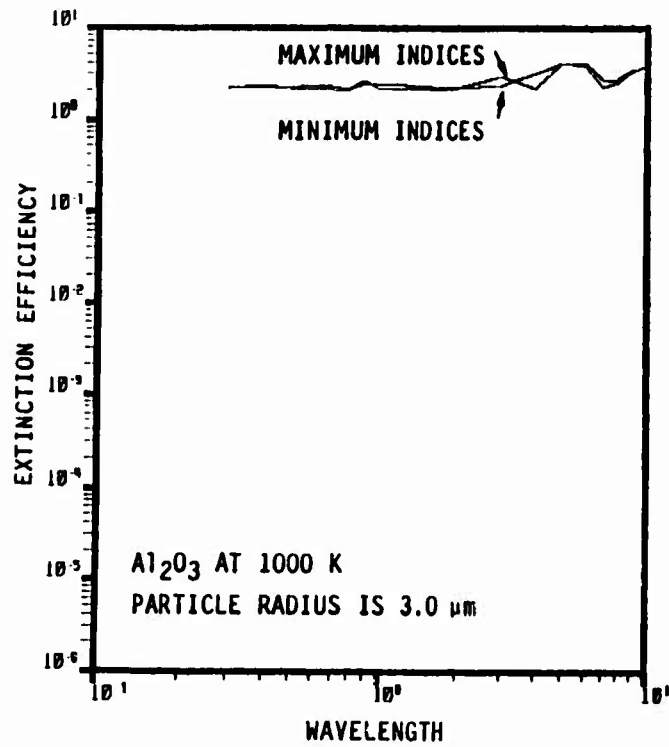
Figure 15. Absorptive efficiency for Al₂O₃ at 1000 K.
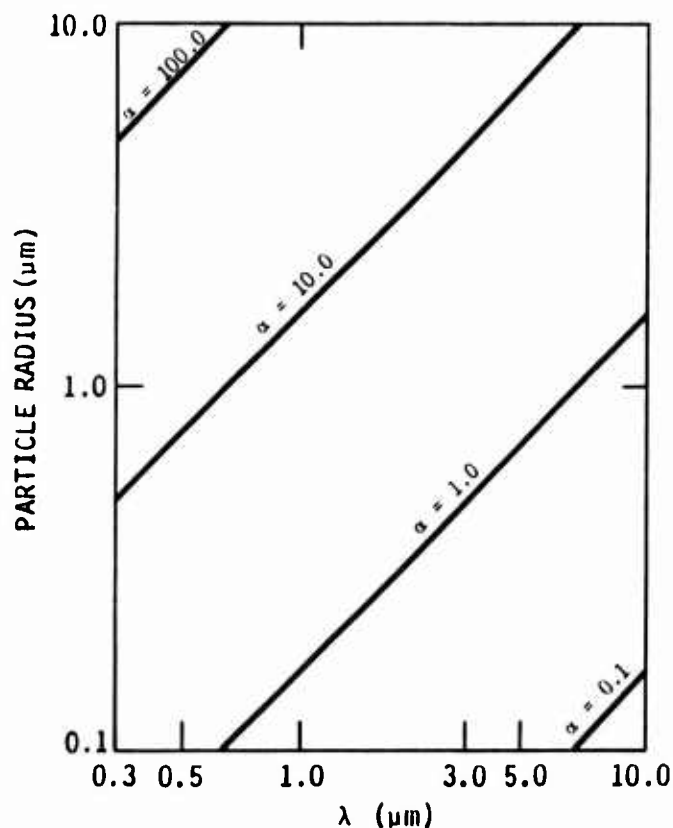

Figure 16. Extinction efficiency for Al₂O₃ at 1000 K.

Figure 17. <u>Mie scattering size parameters, α, as a function
of particle radius and wavelength.</u>

calculations the size parameter combines the effect of particle radius and
radiation wavelength into one parameter, but obscures the fact that the index
of refraction is a function of wavelength only. For a given wavelength, the
optical response of a system can vary due to changes in particle size (i.e.,
size parameter) only. This fact suggests that an optical measurement's
response could be influenced by the size parameter alone. This variation of
response with particle radius (size parameter) can be used to infer specific
information about the refractive index at a given wavelength.

The range of possible extinction efficiencies is given in Figure 18.
Four indices of refraction representative of a large range were used to gener-
ate this figure. The small imaginary indices represent of nonabsorbing mater-
ials and the large imaginary indices represent absorbing materials. The two

37

$$n = 2.0 + 2.0i$$
$$n = 1.05 + 2.0i$$
$$n = 2.0 + 0.1 \times 10^{-7}i$$
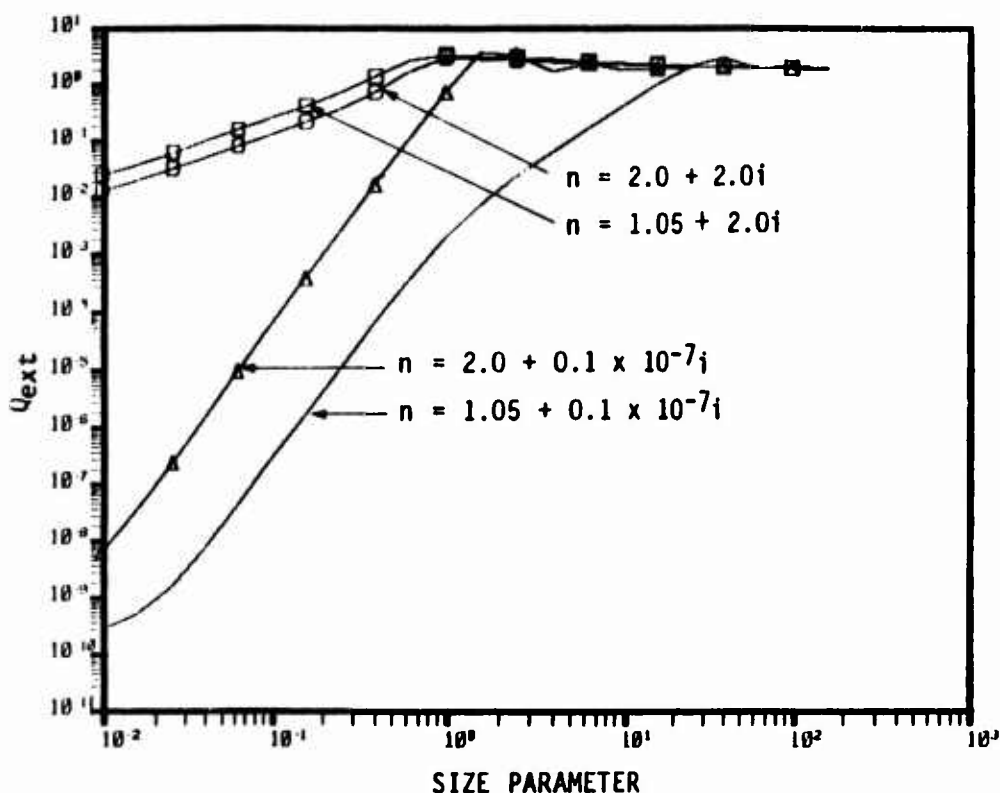$$n = 1.05 + 0.1 \times 10^{-7}i$$

Figure 18. Extinction efficiencies for a wide range in indices of refraction.

real components for the refractive index represent the range typically observed for the real index. The response range is exceptionally large at small size parameters but narrows as the size parameter becomes larger. This apparent insensitivity of the extinction to the refractive index at large values of the size parameter is classically known as the geometric limit. The insensitivity of the extinction efficiency to the optical properties allows extinction data for large size parameters to be used as a direct measurement of the product of number density and particle cross sectional area, Eq. (26).

$$N\pi a^2 \ell = \left(\frac{\ln(I/I_o)}{Q_e} \right) \tag{26}$$

The sensitivity of the extinction measurement to refractive index is further explored in Figures 19 - 23. These figures represent slices of the response surface at constant imaginary or real index for several size parameters. Extinction efficiency is demonstrated to be a function of both the
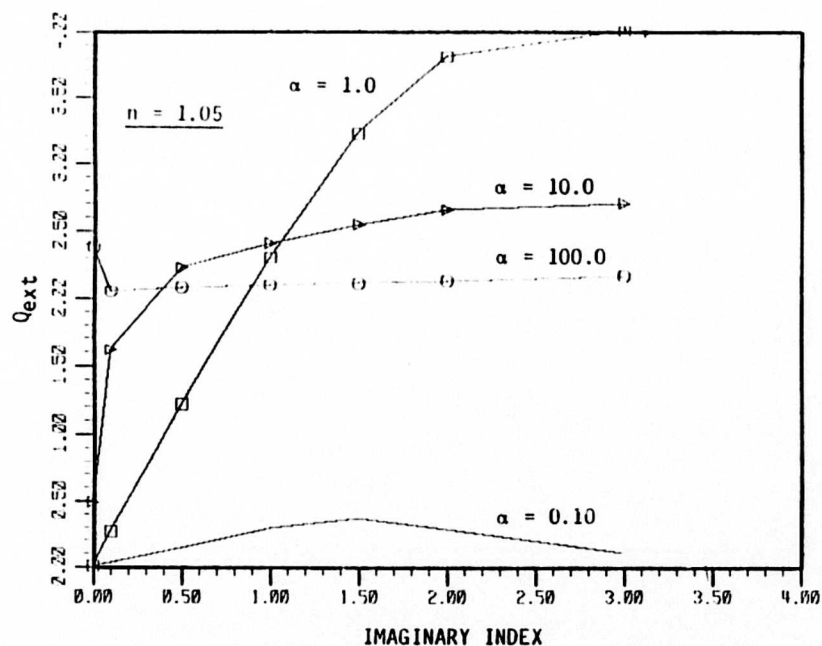
38

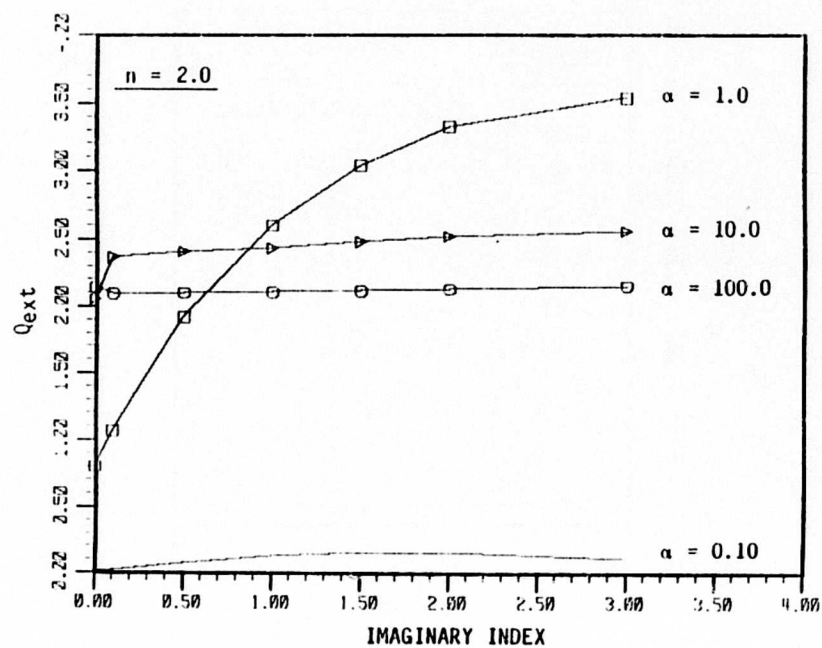Figure 19. Extinction efficiency for real index of 1.05 and variable imaginary index.

Figure 20. Extinction efficiency for real index of 2.0 and variable imaginary index.
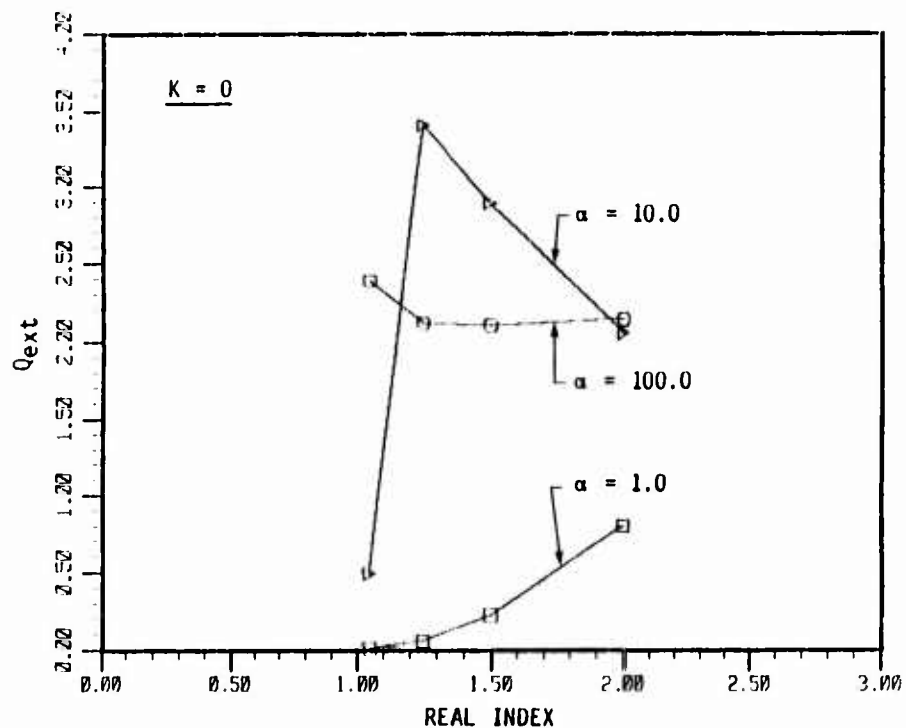
39

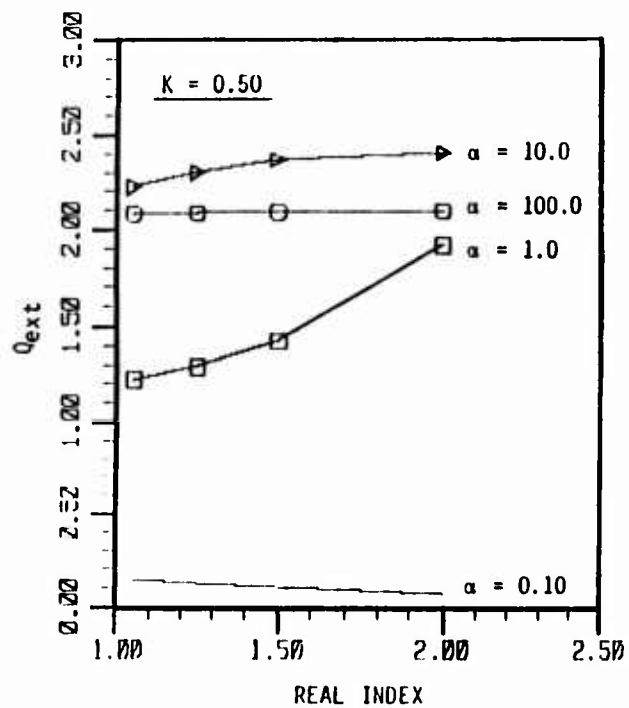Figure 21. **Extinction efficiency for zero imaginary index and variable real index.**

Figure 22. **Extinction efficiency for imaginary index of 0.50 and variable real index.**
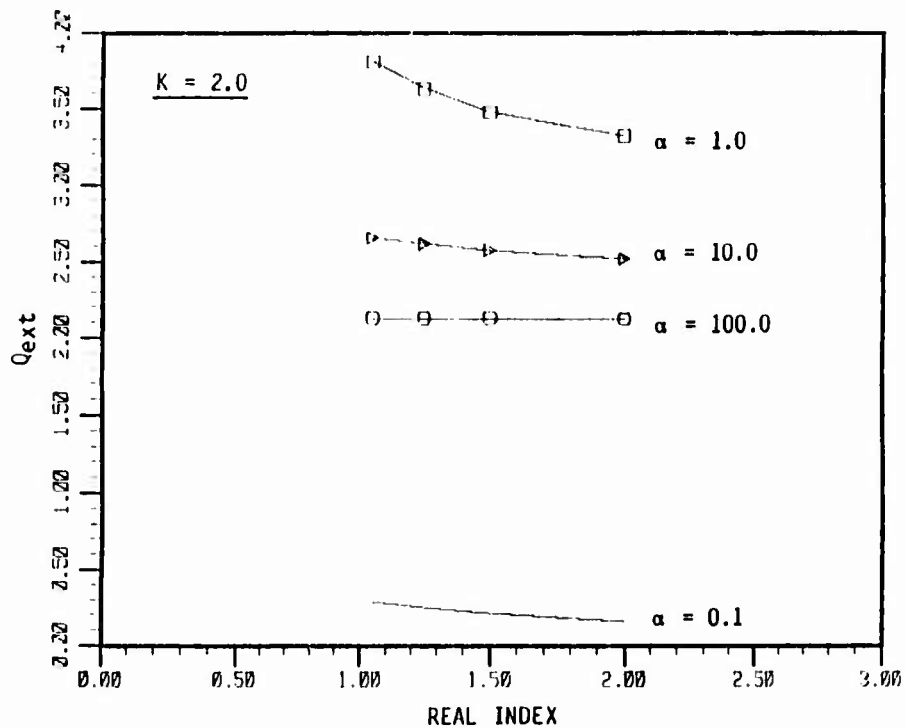
40

Figure 23. Extinction efficiency for imaginary index of 2.0 and variable real index.

real and imaginary indices; it is relatively insensitive to either index for a size parameter equal to 100. This further supports the use of large size parameter measurements to determine the number density-area product. The largest variation in response for a variable imaginary index, as shown by Figures 19 and 20, occurs at a size parameter equal to one. A decreased sensitivity for size parameters other than one is apparent for larger real index values. Figures 21 through 23 illustrate the response range for variable real index at several size parameters; once again, the response is insensitive to the index of refraction at large size parameters. The responses shown in these plots also illustrate a decrease in dynamic range as the material becomes more absorbing and as with the previous set of plots, the highest sensitivity to the real refractive index occurs for a size parameter equal to one. These sensitivity plots show that the extinction efficiency can be used

41

as a measure of the number density cross-sectional area product for large size parameters and is a measure of the real refractive index for size parameters equal to one.

A special note must be made regarding the extinction response for a non-absorbing material as represented in Figure 21. The response range for small values of the real index and size parameter equal to 100 is larger than demonstrated in any of the other cases and could be a error source in a measurement of the number density-area product. Fortunately this combination of refractive indices is physically unlikely for a large size parameter with rocket exhaust particles. A size parameter of 100 only occurs for near ultraviolet wavelengths with our particle size range; the real refractive index in this range is normally greater than 1.4. The large variation in response occurs between 1.05 and 1.2; therefore, extinction is still a reasonable measure of the number density-area product for a nonabsorbing material. In an actual experimental system, the final indices that are determined would be used to verify this assumption.

A similar study of absorption efficiencies and their dependence on size parameter and refractive index is given in Figures 24 through 27. The case of a zero imaginary refractive index has been omitted since a zero imaginary index indicates a material with no absorptive properties. The first two plots show the variation of absorption efficiency with imaginary index. Once again the most dramatic response range is found for a size parameter equal to one. However, there is no area of insensitivity, as there was with extinction. This indicates that emission measurements over the entire range of refractive index will yield information about the imaginary index. Figures 26 and 27 show the response of the absorption efficiency to the real index. It is not surprising to find that the emission response range, represented by the absorptive efficiency, is not as dramatic as for the imaginary index. In summary, emission measurements will be primarily dependent on the imaginary index and secondarily dependent on the real index.
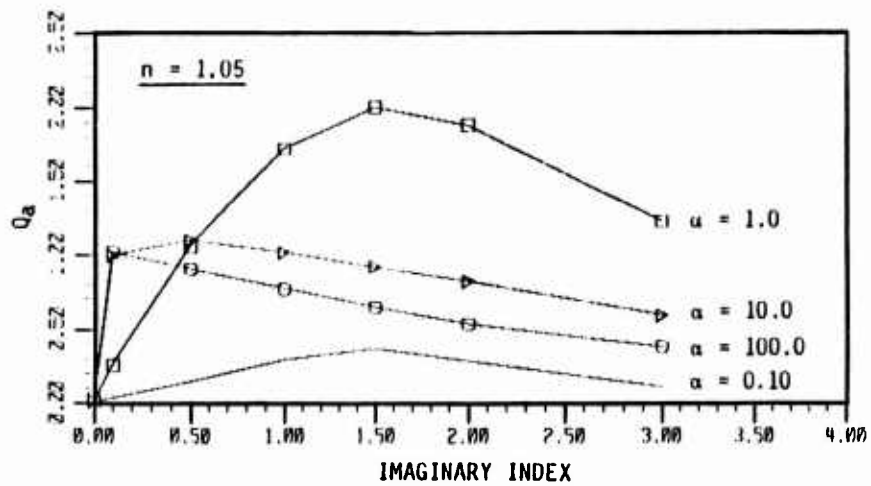
42

Figure 24. Absorption efficiency for real index of 1.05 and variable imaginary index.
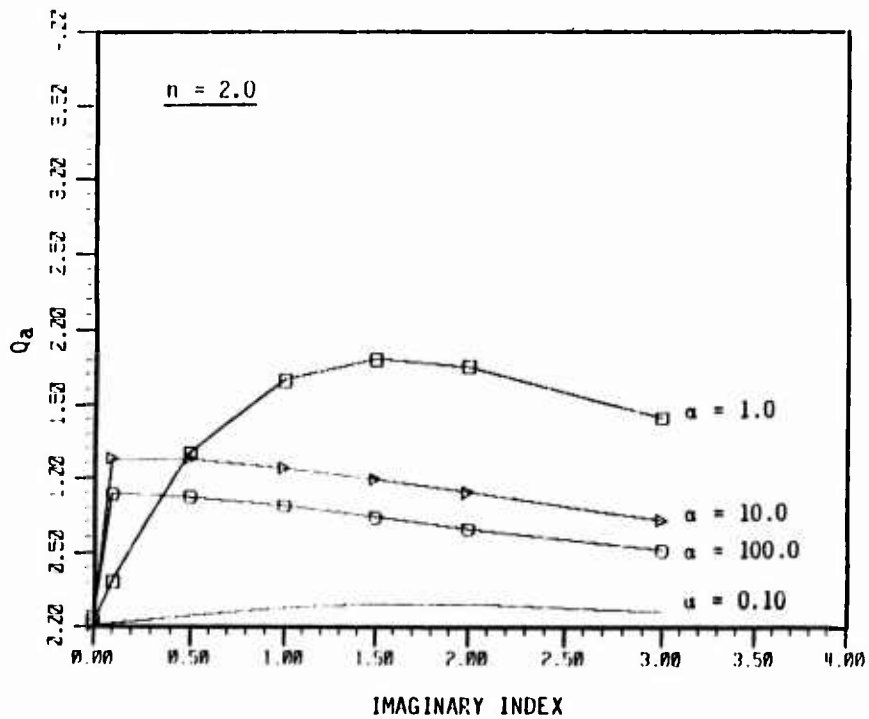

Figure 25. Absorption efficiency for real index of 2.0 and variable imaginary index.
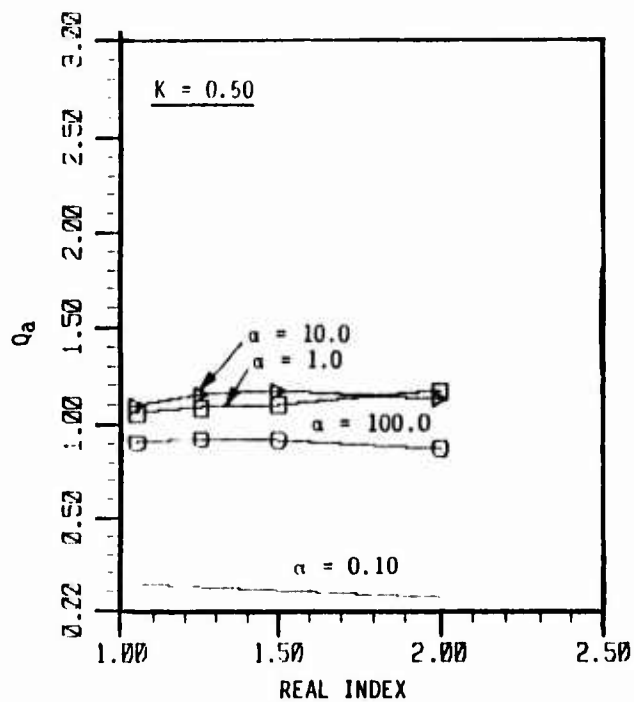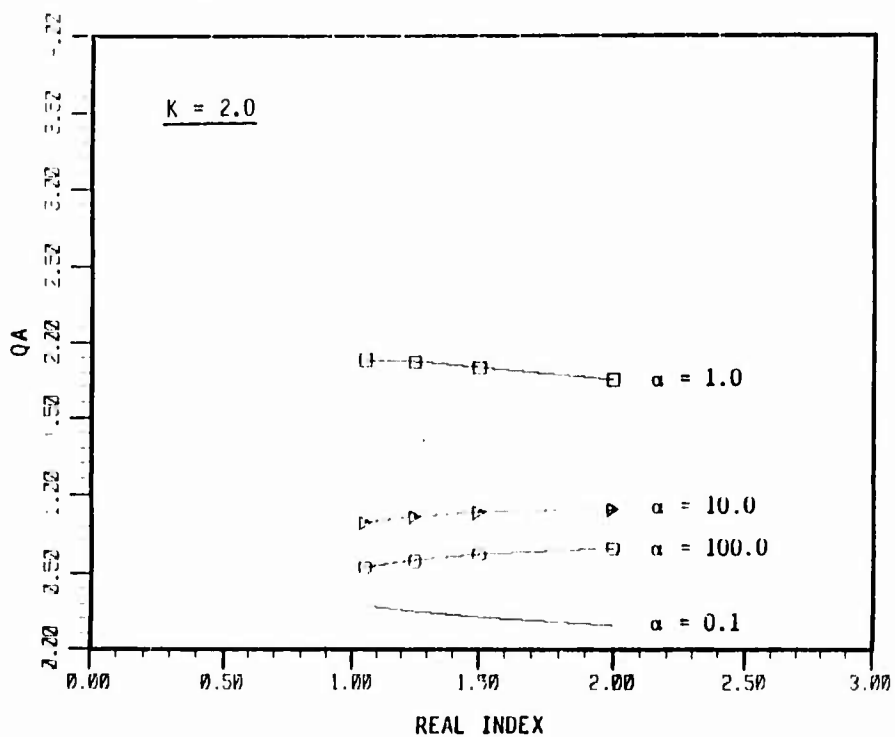
43

Figure 26. Absorption efficiency for imaginary index of 0.50 and variable real index.

Figure 27. Absorption efficiency for imaginary index 2.0 and variable real index.

The previous discussion has examined the sensitivity of the extinction and emissive response of systems of particles to the refractive index of the materials. The conclusions from this study are summarized in Figure 28 which presents extinction and emission sensitivities grouped by size parameter range. For large size parameter values, the extinction measurement can be used to determine the number density-area product for the system and the emission measurement is a reasonable measure of the imaginary refractive index. When $10 > \alpha > 1$, the extinction measurement becomes sensitive to the real and imaginary indices, and the emission measurement is sensitive to the imaginary and real indices. When $\alpha < 1$, both measurements are sensitive to the imaginary and real indices.
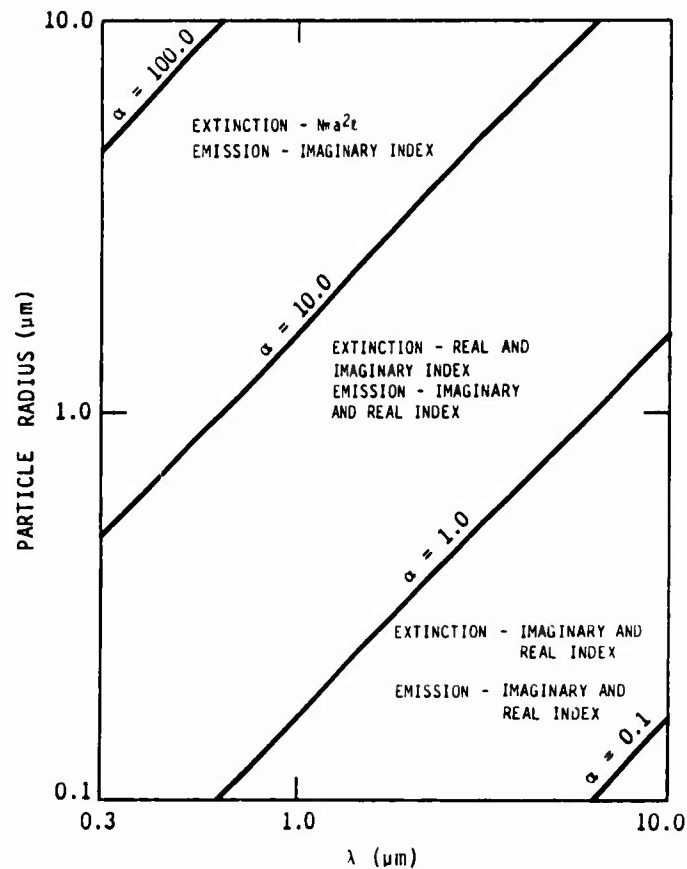

Figure 28. Extinction and emission measurements and their sensitivities.

45

3.1.2 <u>Scattering Measurements</u> - The scattering response is a function of angle and polarization in addition to size parameter and index of refraction. Due to the complexity of the scattering response, several measurement types must be considered along with their sensitivities to the refractive index. These measurements may be compactly represented by the polarization ratio and the angular intensity of scattered natural light.

Figures 29 through 32 display the polarization ratio as a function of angle for four refractive indices at each of four size parameters. Polarization ratio is defined in Eq. (27).

$$\bar{P} = \frac{\left(I_{||} - I_{\perp} \right)}{\left(I_{||} + I_{\perp} \right)} \tag{27}$$

where

$\bar{P}$ - polarization ratio

$I_{\perp}$ - perpendicular intensity

$I_{||}$ - parallel intensity

Figures 29 and 30 show an insensitivity of response to the refractive index for size 0.1 and 1.0. At larger size parameters the response becomes dependent on the refractive index in addition to becoming a highly structured function of angle, as shown in Figures 31 and 32. The degree of structure in these responses implies that although in principle refractive index influences the response, measurements based on these predictions would be very prone to error due to the large response changes for small changes in angle. The structure becomes more detailed for a size parameter of 100, but the response becomes sensitive to the imaginary index.

The shift in the function from a size parameter of 1.0 to 10.0 also suggests that the measurement could be used to diagnose the size of the particles in the dispersion. However, this measurement would be useful only in the size range where the response function is making the transition from the invariant curve for a size parameter of one to the robust function for size parameter equal to ten.
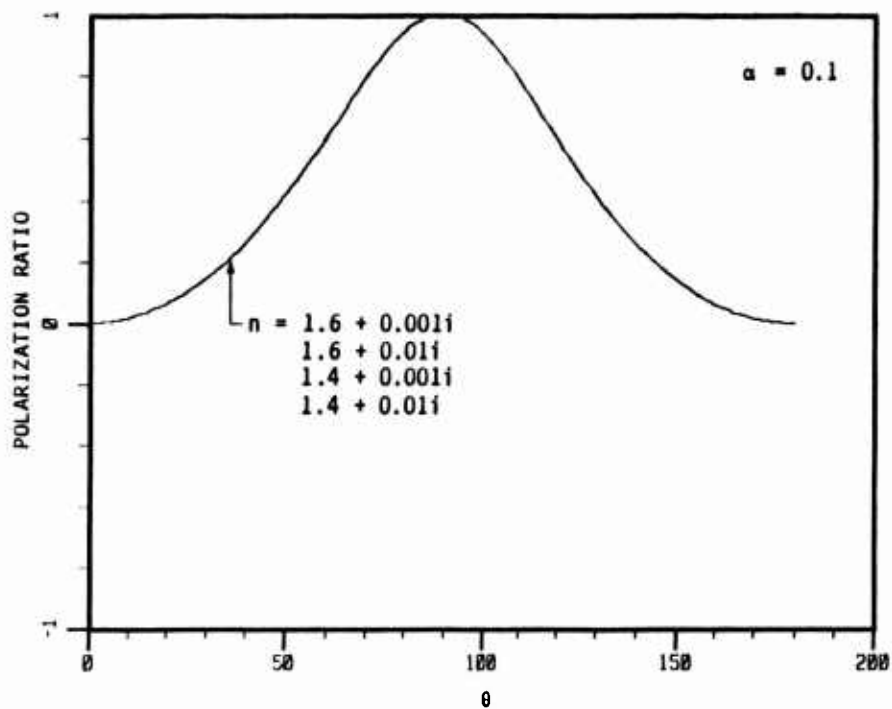
46

Figure 29.   Polarization ratio for a size parameter of 0.1.
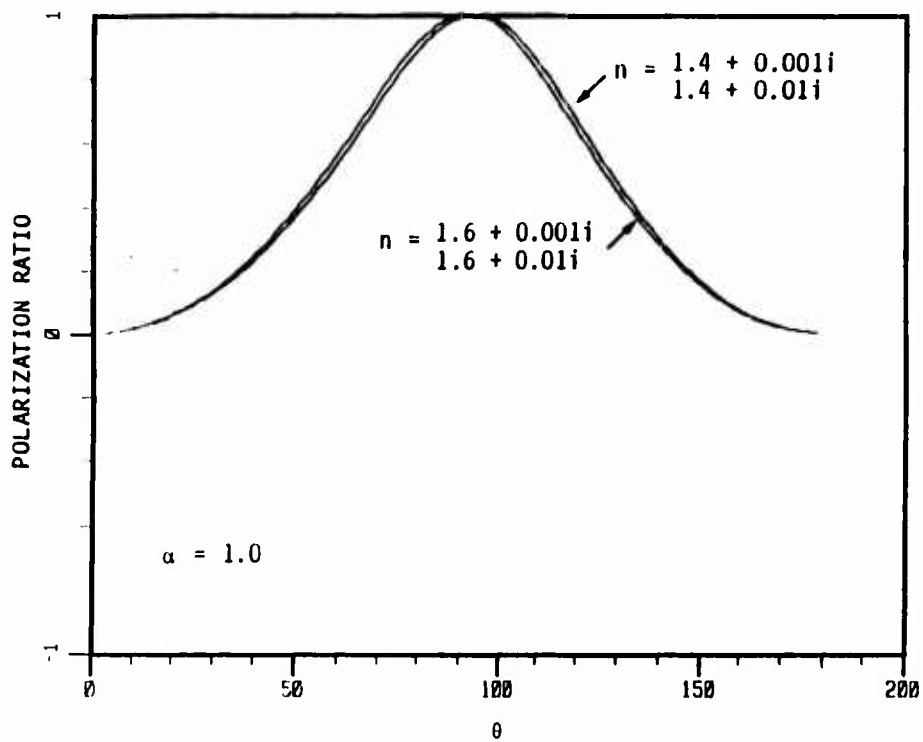

Figure 30.   Polarization ratio for a size parameter of 1.0.
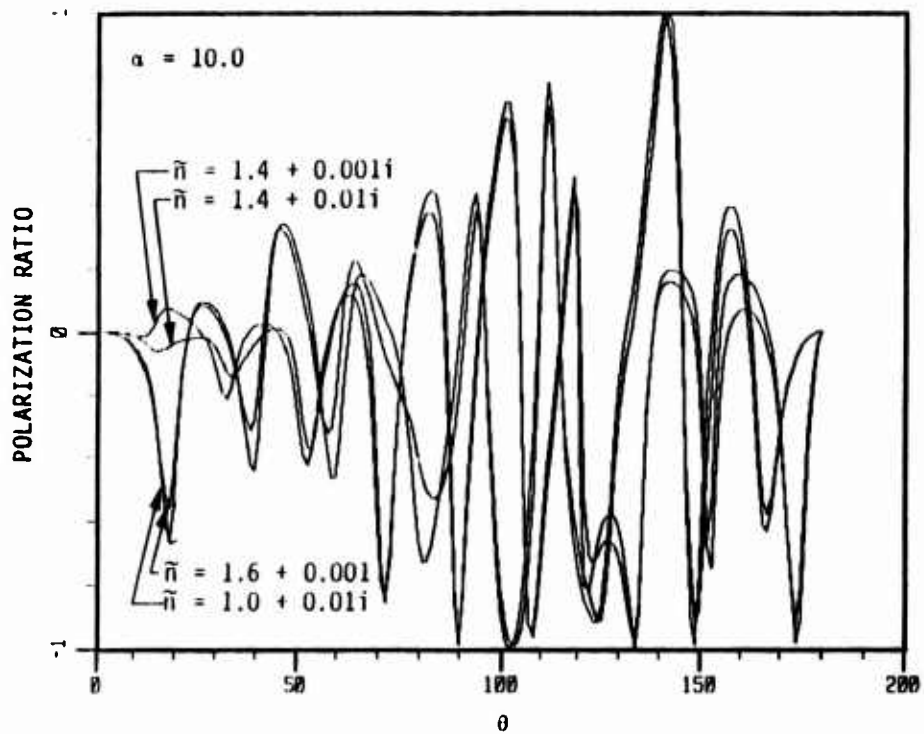
47

Figure 31. Polarization ratio for a size parameter of 10.0.
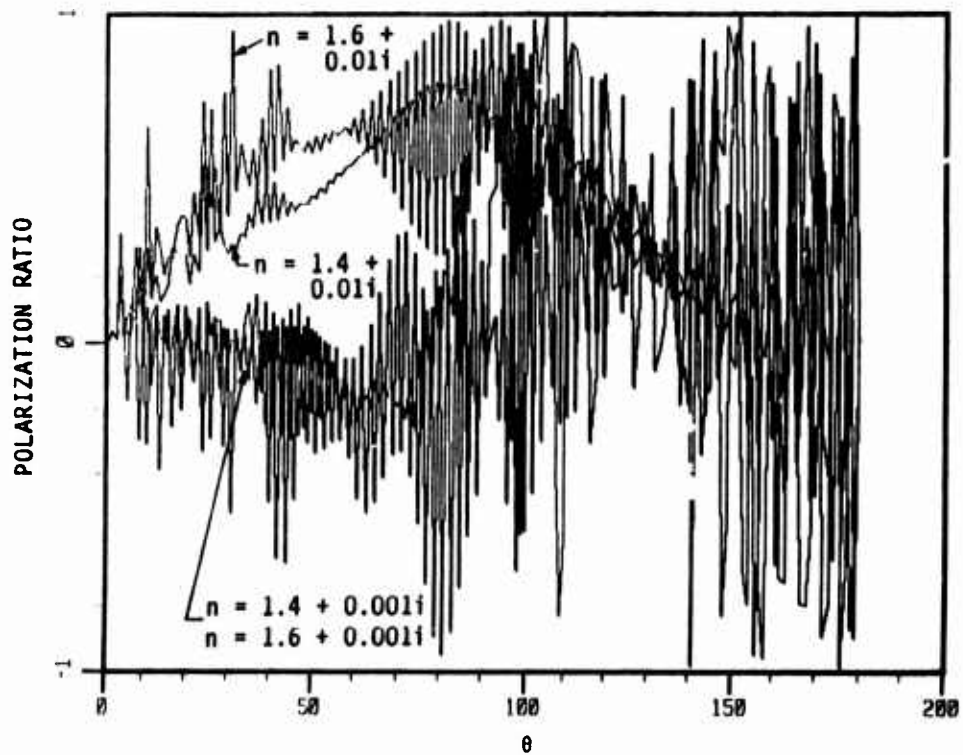
Figure 32. Polarization ratio for a size parameter of 100.0.

48

The possible uses for scattering polarization measurements are summarized
in Figure 33. This shows that the measurement is insensitive to particle size
or refractive index for size parameters less than 1.0. For size parameter
between 1.0 and 10.0, the measurement could be used for sizing or as a measure
of refractive index, but it is exceptionally sensitive to angular position.
At size parameters between 10 and 100 the responses become sensitive to the
imaginary index but are still dependent on angular position.
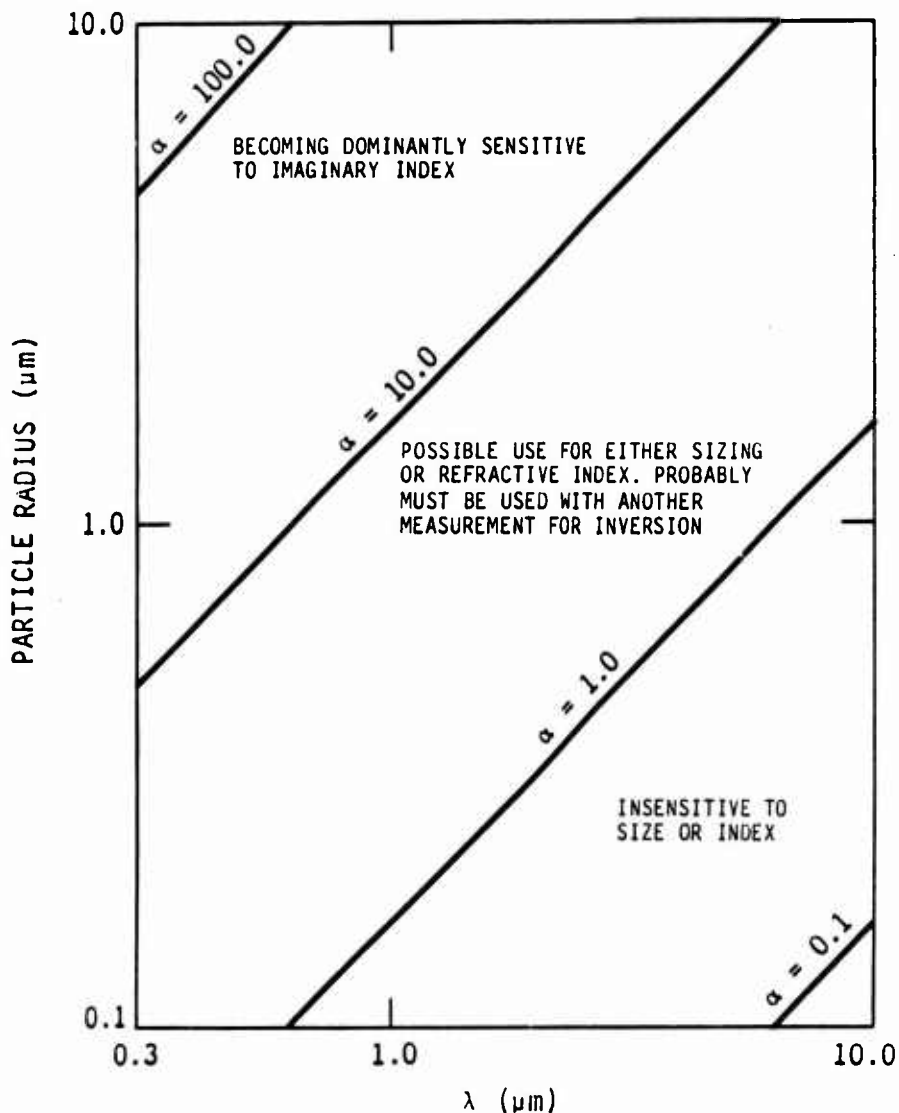
Figure 33. Polarization sensitivity.

Scattered intensity of incident natural light forms the other type of scattering measurement that can be made. These measurements can be either absolute intensity determinations at a specific angle or a ratio of intensities at two or more angles. The latter measurement type has the advantage of being independent of the number density-area product for the particle dispersion. Plots of intensity as a function of angle for four indices of refraction are given in Figures 34 through 37 for size parameters 0.1, 1.0, 10.0 and 100. The intensity distribution is a well behaved function for size parameters 0.1 and 1.0. In addition, the influence of the two refractive indices on the response is apparent. The real index dramatically affects the magnitude of the response and the imaginary index has almost no effect on the response at all. The curve shape, commonly called the dissymmetry ratio, is represented by the ratio of intensities at two angles and is insensitive to the refractive index. However, this ratio is reasonably sensitive to the size parameter and could therefore be used as a diagnostic tool for particle size at a fixed wavelength. For a size parameters of 10.0, represented by Figure 36, the uses for scattering measurements become much less clear; the angular intensity function becomes much more structured and its use as a diagnostic aid becomes more tenuous. As with the polarization ratio, the highly structured curve, although sensitive to the refractive index in some regions, is difficult to use for determinative purposes. As an example, the first scattering lobe for the size parameter equal to 10.0 is reasonably sensitive to the real refractive index. However, any intensity determination at a specific angle would require a very high degree of accuracy in specifying the exact angle for the scattering because of the function's large slope in this region. Therefore, the scattering measurement is not a good diagnostic aid for the refractive index at high size parameter values.

Finally, the intensity distribution for a size parameter of 100.0 is shown in Figure 37. The salient features of this plot are a fine scale structure superimposed on a larger scale function variation. The response sensitivity for this size parameter has shifted to the imaginary index in the first ninety degrees of the function.

Figure 34.   Scattered intensity for size parameter of 0.1.
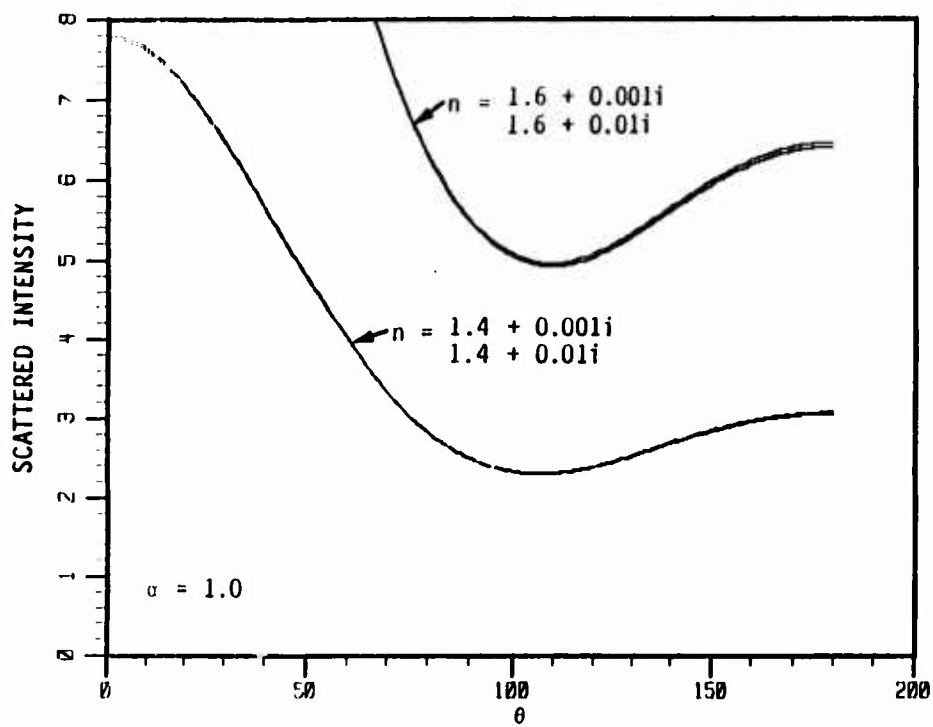
Figure 35.   Scattered intensity for size parameter of 1.0.

51
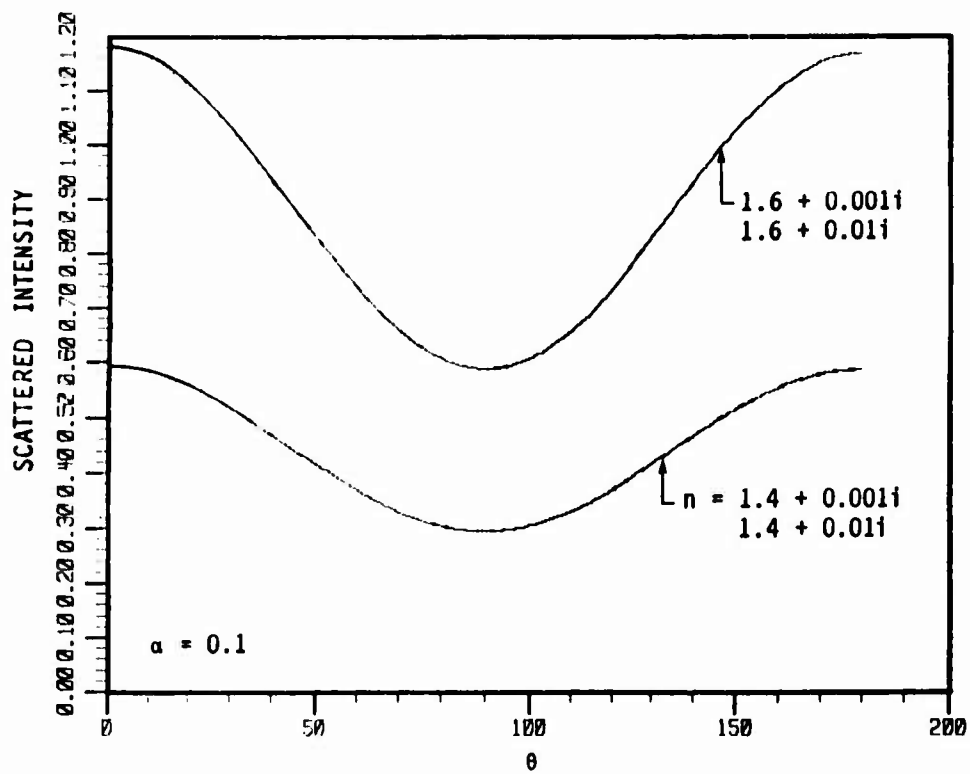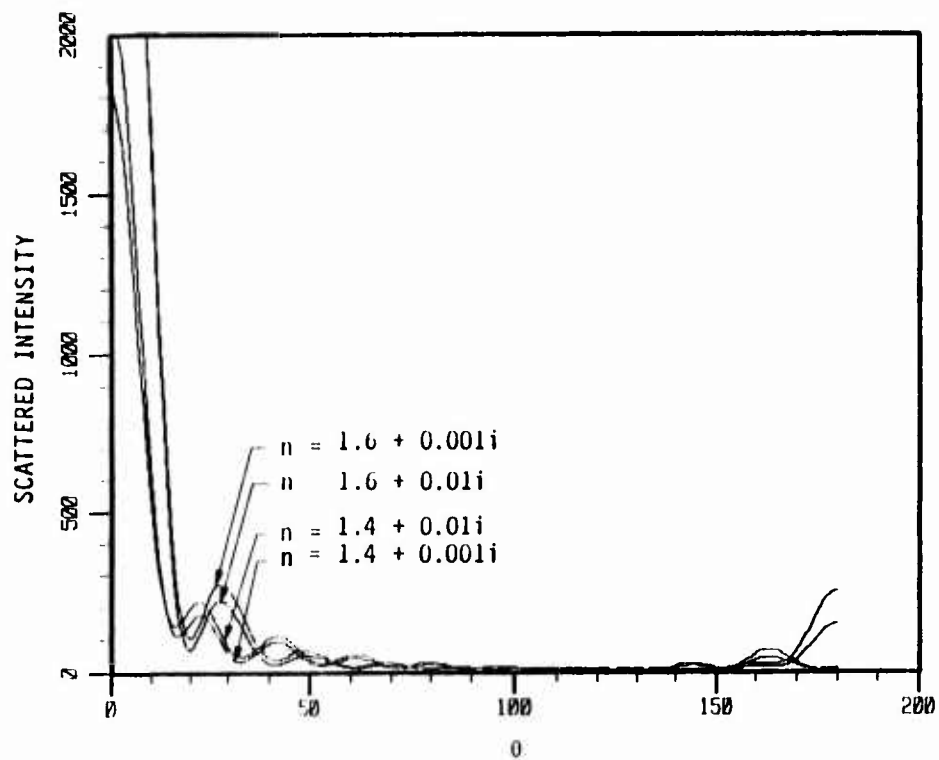
Figure 36. Scattered intensity for size parameter of 10.0.
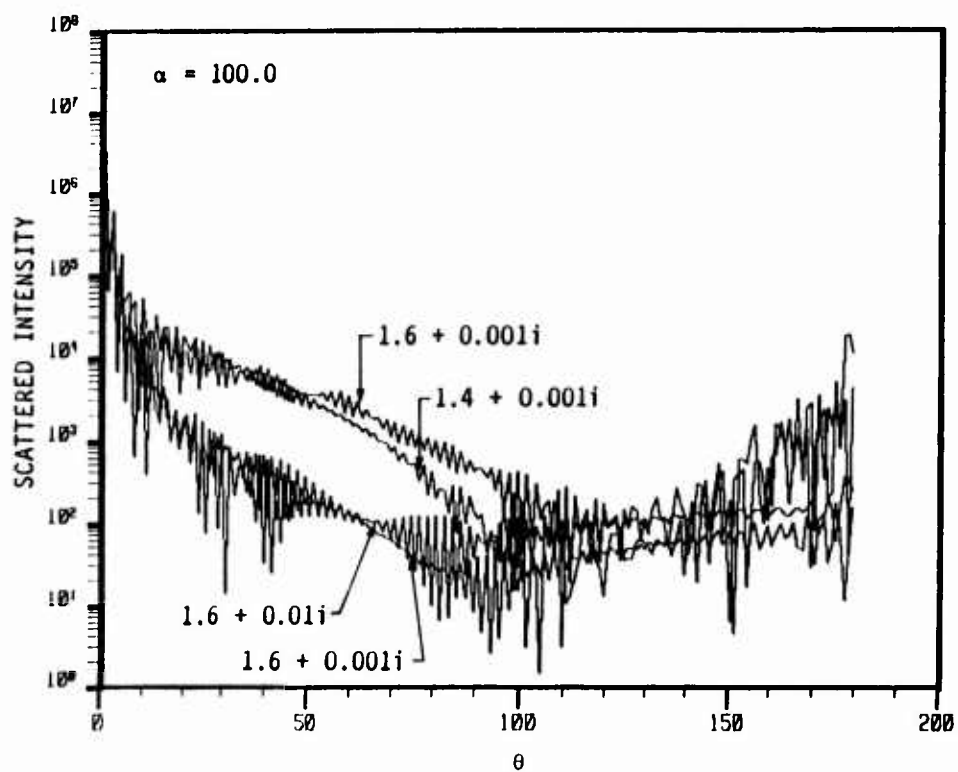
Figure 37. Scattered intensity for size parameter of 100.0.

Scattering measurements and their utility are summarized in Figure 38. For size parameters between 0.1 and 1.0 the intensity function is well behaved and sensitive to the real index. The shape of the curve is sensitive to the size parameter. For size parameters between 1.0 and 10.0, a transition occurs to a structured function that is sensitive to the real index in the first lobe of the function. At larger size parameters, the scattering becomes even more structured and the sensitivity shifts to the imaginary index in the first ninety degrees of scattering.

Figure 38. Scattering intensity sensitivities.

3.2 Data Inversion: Determination of the Refractive Index

The measurements discussed in the previous section can be used to determine the refractive index of the particles in a dispersion. In principle, three unknowns will be present for any system of particles, the two components of the refractive index and the number density-area product. Since the refractive index is dependent on the wavelength only and not the part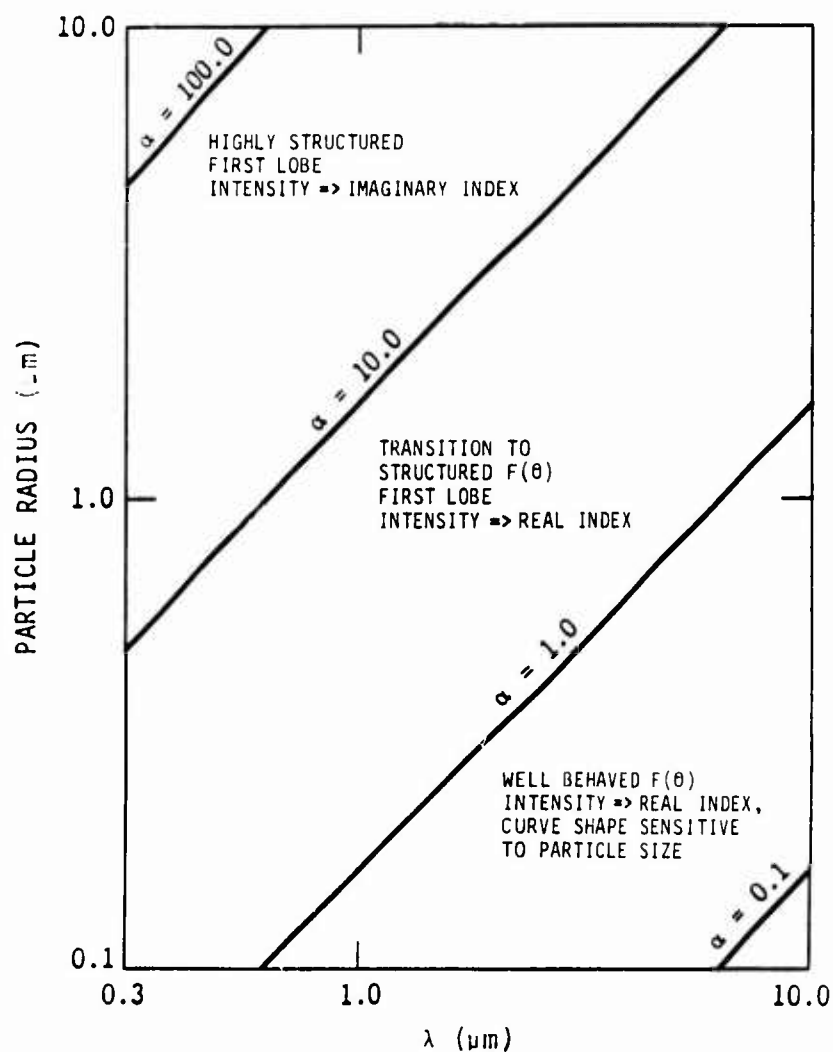icle size, several experiments with the same material but different size particles may be used to for data inversion. The results of several experiments are thus used in concert to determine the refractive index.

The most direct measurements, as presented in the previous section, are extinction and emission. In general, these two measurements will form the backbone of the experiment. Where necessary, scattering measurements can be used to fill data gaps. The sensitivity variation with size parameter can be used to good advantage. The key to determining of the refractive index is to use the extinction as a measure of number density-area product where it is insensitive to the refractive index. This will be in the near ultraviolet for large particles as shown in Figure 39. Given this absolute determination of the number density-area product, emission and extinction measurements at other wavelengths are indicative of the refractive indices at these wavelengths. In a sense the experiment is based on the transition of sensitivity with decreasing size parameter. The results of experiments at smaller particle sizes are then used in conjunction with the large particle experiment to determine the refractive index over a large wavelength range.

An indicative example is given by a two experiment system: one for particle sizes of 10 μm and one for particle sizes of 0.3 μm. For the 10 μm particle size experiment, the short wavelength extinction measurements give the number density area product. At longer wavelengths the extinction and emission measurements can be used to infer the refractive index. This procedure of inferring the indices of refraction based on the optical response uses the Mie calculations and is subject to the sensitivities associated with the size parameter; as the size parameter decreases, the results are more
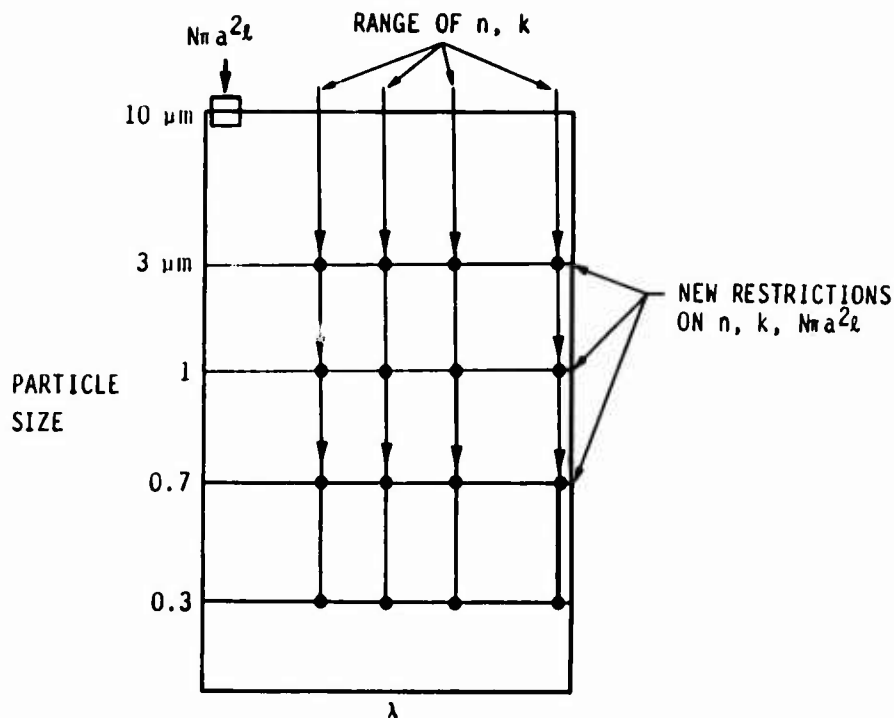
Figure 39. Multiple experiment determination of refractive index.

sensitive to the refractive index. At 10 μm the emission measurement is rea-
sonably sensitive to the imaginary index and the extinction measurement yields
a range for the real index. These results are used in conjunction with those
of the 0.3 μm particle experiment. The refractive index range for a 10 μm
wavelength, from the 10 μm particle experiment and the extinction and emission
measurement at 10 μm from the 0.3 μm particle experiment yields a range for
the number density-area product for the dispersion of 0.3 μm particles. Thus,
the results from the 10 μm particle experiments are used to tie down the num-
ber density-area product for the 0.3 μm dispersion. Measurements at other
wavelengths are used to infer the refractive index at those wavelengths and
the results of the two experiments intersect to produce a smaller range of
possible indices. Additional experiments at other particle sizes can then be
done. One of two methods is used to determine the number density-area product
for the system: either the extinction at short wavelengths or the refractive
index at long wavelengths. The method which provides the greater accuracy is
the one which is chosen.

As a further illustration of the multiple experiment data inversion process, two simulated inversions have been performed: one for alumina and one for carbon. The index of refraction data base which was previously discussed was used to produce mock experimental data. Appropriate experimental error bars were added to these numbers, and an inversion was performed within the limits of experimental uncertainty (error bars were ±1 percent for extinction measurements and ±7 percent for emission measurements, these errors are indicative of a very carefully performed experiment). The results are shown in Figure 40 for four experiments for each system, 10.0 µm, 3.0 µm, 1.0 µm, and 0.7 µm. The solution for each system is in the form of a solution region. The refractive indices within these regions represent an extinction and emission response range that is of the same order as the extinction and emission errors for the most sensitive experiment. Each of these results, for the refractive index at 10 µm is representative of an extinction and emission response range of approximately ±1 percent and ±7 percent plus the error involved in the number density area product, typically 1-5 percent. It is interesting to note the decrease in sensitivity for high values of the real index. This is exemplified by the much larger range in imaginary and real index for carbon and was previously mentioned as a part of the sensitivity study portion of this report. However, each of these solution regions is representative of the same range in extinction and emission response of a system of particles.

Finally, it must be pointed out that the process of inverting the data is a two-dimensional iteration process. The extinction and emission are dependent on both refractive indices, and the solution process, from an extinction or emission response to the refractive index, is iterative in nature. For a large experimental program this data reduction process would have to be automated; a two-dimensional bisection solution process as used by Parker (Ref. 29) would be appropriate.
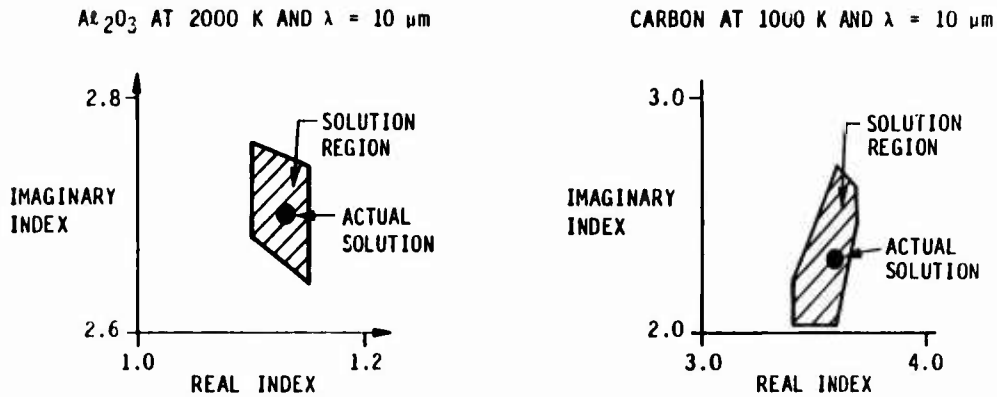
Figure 40.   Data inversion results for the refractive index.

3.3   Particle Size and Shape Effects

The analysis so far in this report has ignored the effects of disperse particle size distributions and particle shape.   The effect of a particle size distribution is easily accounted for while the effect due to particle shape is a little more tenuous.   In general, a particle size distribution merely represents a complication in the calculation procedure.   The optical response must now be considered to be that of a sum of particles which have a range in radii and efficiency corresponding to the size distribution of the particles.   If the system is optically thin, the response is simply the sum of the responses for the varying size particles, i.e., an integral of emission or extinction over the size distribution is appropriate.   The important aspect of size distribution effects is knowing the appropriate size distribution for the system. An unknown size distribution can catastrophically affect the error in the experiment.

Figures 41 through 45 illustrate the effect of a size distribution on the extinction and absorbtion efficiencies for a particle system.   Figure 41

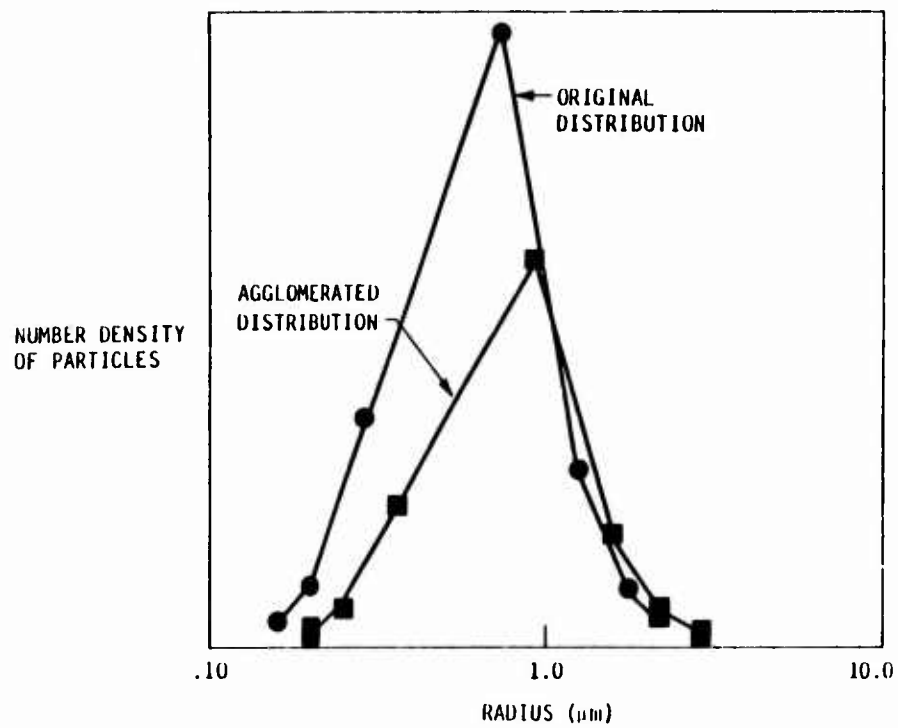Figure 41.   Nominal 1 μm size distribution and agglomerated distribution.
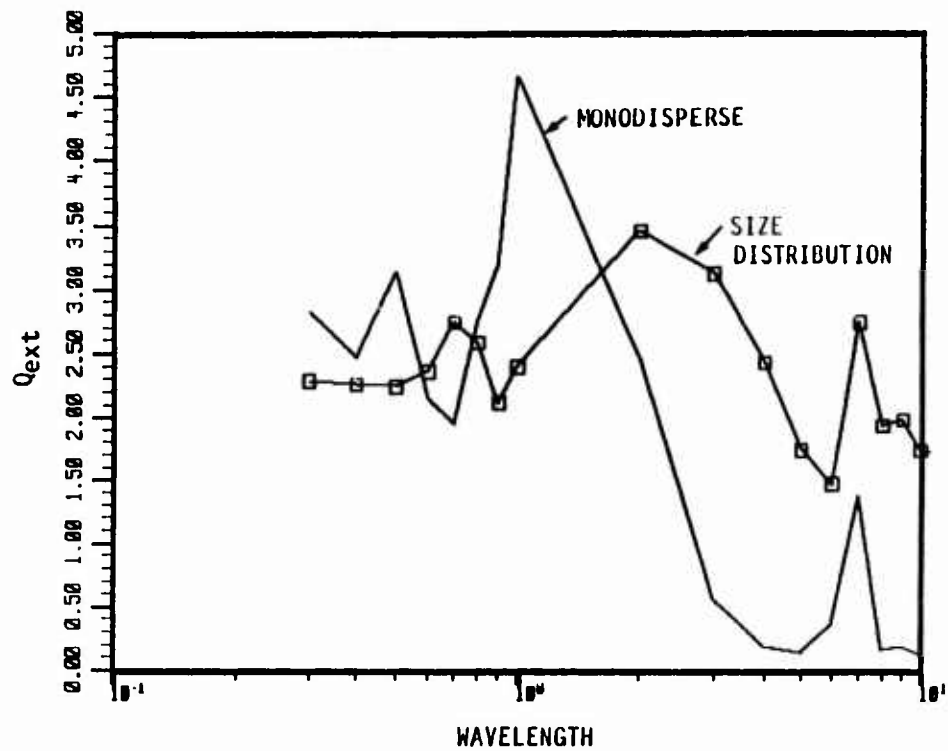
Figure 42.   Extinction efficiency for a monodisperse and size distribution type systems.
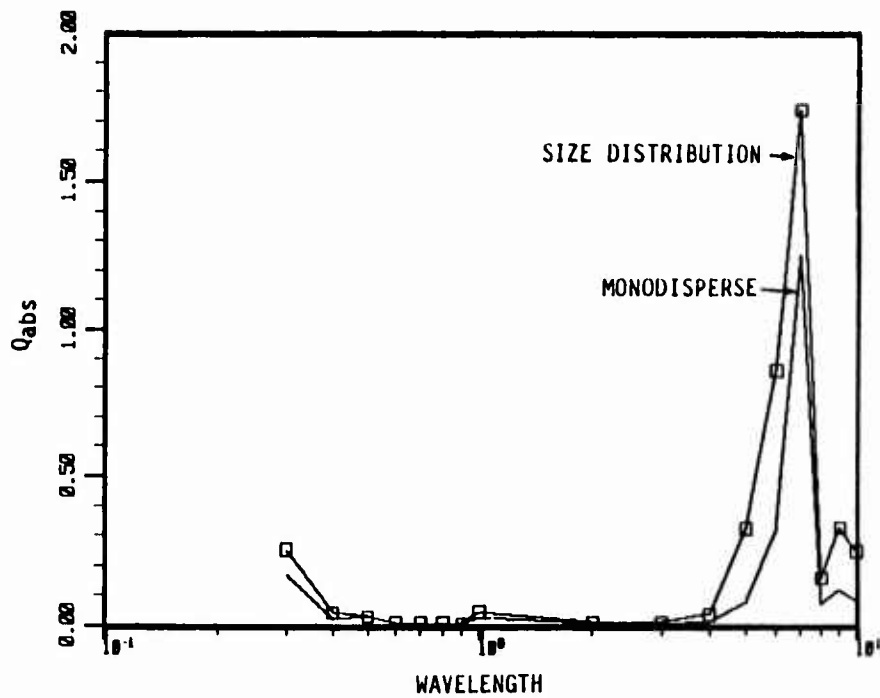
Figure 43. **Absorption efficiency for a monodisperse and size distribution system.**
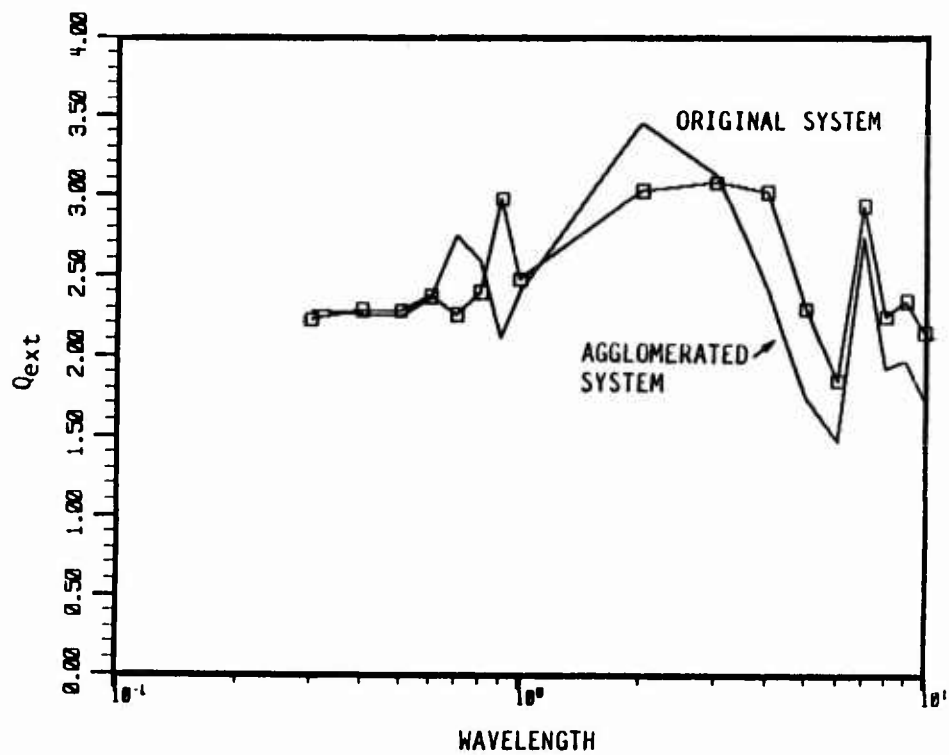
Figure 44. **Agglomeration effect on extinction.**
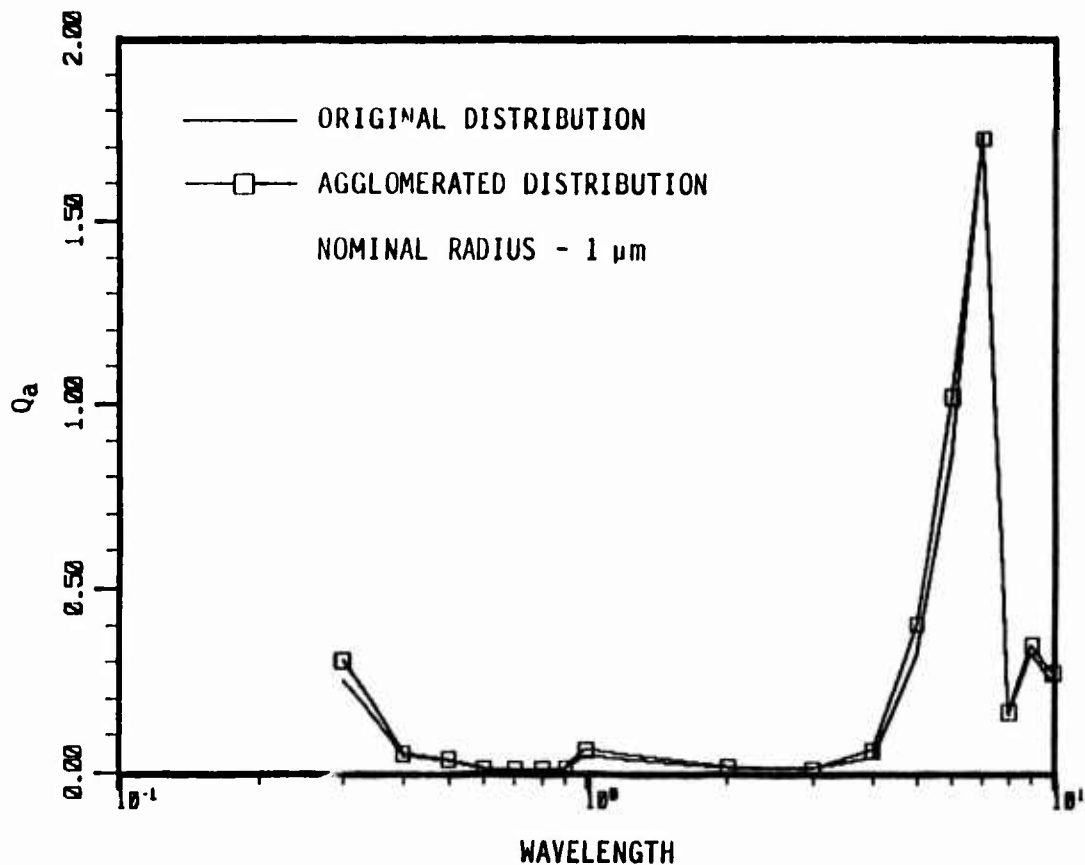
Figure 45. Agglomeration effect on absorption.

shows a nominal 1 µm distribution (as opposed to a monodisperse 1 µm system). Figures 42 and 43 show the effect of the size distribution on the area weighted average extinction and absorption efficiency; the extinction efficiency is exceptionally sensitive to the change from a monodisperse system to a size distribution. An agglomerated system has also been modeled. This system was produced by assuming that the total number of particles was reduced by a factor of 2. The size was accordingly shifted upward by the cube root of 2. This is not an extreme agglomeration model. In some systems there is a tendency to agglomerate to one specific size. The effects of the agglomeration are shown in Figures 44 and 45. Once again the extinction efficiency is reasonably sensitive to the change in size distribution while absorption efficiency is almost unaffected. An additional error from agglomeration is a possible change in shape.

The solution to the error caused by particle size distributions is to always know the distribution of particles in the experimental system. This knowledge can be obtained with pre- and post-experiment SEM particle studies, and by using scattering dissymmetry as a diagnostic indicative of size. The size distribution of the particulates can be improved toward the ideal of a monodispersion by pre-sorting the particles. This sorting could be performed in a cascade impactor due to the small sample quantities required.

Particle shape effects are much harder to quantify; strict Mie theory assumes perfect spherical particles and the optical response deviation due to particle shape is not well quantified. However, recent work by Pinnick et al. (Ref. 30), has experimentally determined for pure scatterers with a real index of 1.54 that random particle shape has very little effect on the optical response for systems of particles except for scattering at angles between 30 and 180 degrees with size parameters greater than 5. Therefore, our extinction and emission measurements will be largely unaffected by particle shape.

3.4 Measurement Recommendations

The sensitivity analysis and data inversion study have identified which measurements can be used in which size regimes to produce information relevant to the refractive index. This information is summarized in Figure 46. Note that in all size regimes the two primary measurements are extinction and emission; the quantity to which the measurement is sensitive may change, but for all sizes these two measurements are useful. Scattering can be used in the small size parameter range as a diagnostic aid for real refractive index and size. It is theoretically useful in the larger size regimes, but the degree of structure in the angular distributions would make data analysis inversion and analysis extremely error prone. Given these trends, the measurements listed in Table 8 are recommended, in order of preference, as the primary diagnostics for this refractive index study.

61
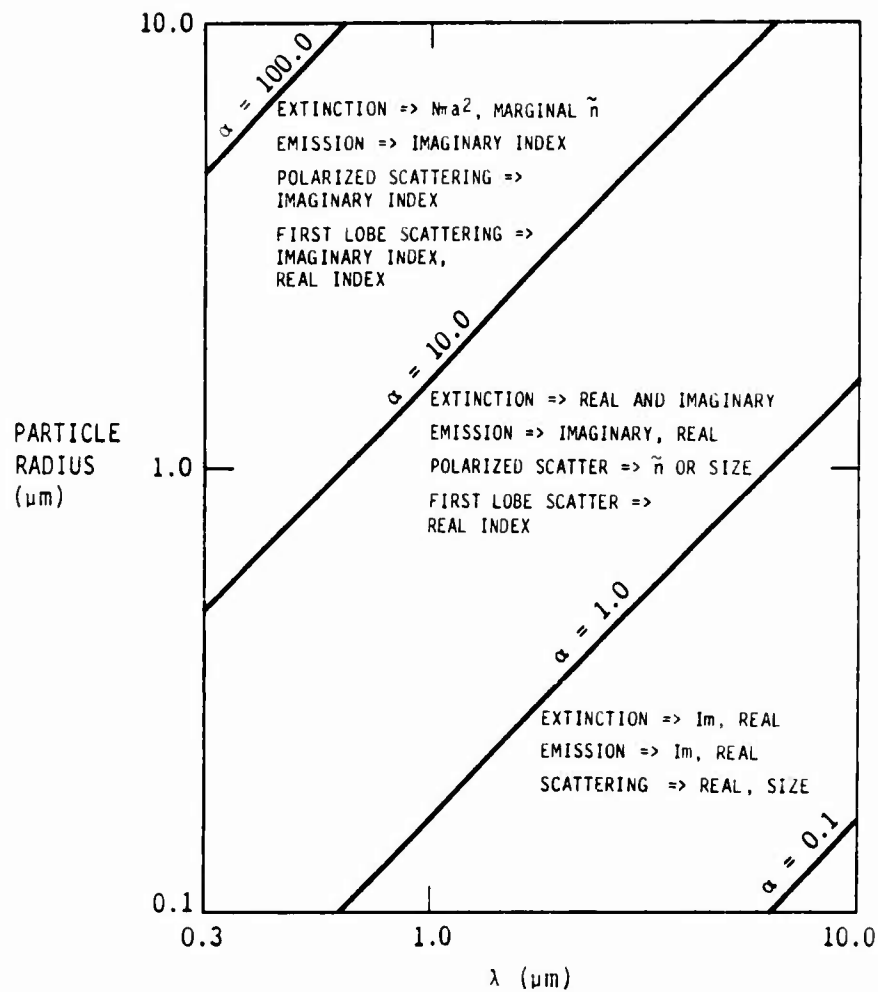
Figure 46. **Optical measurement sensitivity summary.**

TABLE 8. Measurement recommendations.

• Extinction	=> $N\pi a^2 \ell$	
	n,k	
• Emission	=> n,k	
• Scattering Assymetry	=> size information for $\alpha < 1.0$	
• Absolute Scattering	=> real index $0.5 < \alpha < 5.0$	

4. DIAGNOSTIC MEASUREMENT TECHNIQUES

4.1 Requirements and Proposed Approach

From the preceding discussion it is clear that diagnostic techniques must be developed in two areas. The primary requirement is the capability to simultaneously acquire extinction, emission, and scattering measurements over a broad wavelength range, i.e., $0.1 \mu m \lesssim \lambda \lesssim 10 \mu m$, within a time duration determined by a shock tube test time. Secondly, techniques are needed for characterizing aerosol number density and particle size. While information on number density and particle size can be unfolded from the extinction and scattering data, it is useful to consider additional techniques that can provide such information independent of a particle optical properties.

The approach we have chosen to meet these objectives is to design a shock tube experiment implemented with numerous spectroscopic and radiometric measurements that can be deployed simultaneously on each shot. A discussion of the proposed measurement techniques is presented below.

4.2 Description of Proposed Diagnostic Techniques

4.2.1 Particle Number Density and Size Characterization - In the previous chapter, it was shown that with the appropriate choice of particle size parameter, α, (where $\alpha = 2\pi a/\lambda$) extinction and selected scattering measurements can be used to infer information on particle number density and, to a more limited extent, check assumptions on particle size distribution. For example, at large size parameters ($\alpha > 10$) extinction efficiencies become independent of particle size and, to a great extent, of refractive index. Thus, measured extinction signals can be useful for determining line-of-sight number densities. At intermediate-to-small size parameters, angular scattering distributions can provide information on particle size (see Figures 34 through 37). Thus, to the extent it is practical, particle size and wavelength should be varied in the experiments and analysis of the observed extinction and scattering signals could be used to infer particle number density and size information.

63

A second technique which should be used to characterize particle size distribution is to perform micrographic particle sampling/sizing both prior to particle loading and subsequent to shock heating. Scanning electron micrography in addition to optical micrography is recommended. Post-test analysis of the shock heated particulates is useful for establishing limits on possible effects due to particle agglomeration and/or particle fragmentation in the shock tube.

Finally, it is recommended that high resolution snapshots of the particle field behind the shock also be taken. An attractive technique is to take short exposure ($\tau_{exposure}$ < 20 ns) holograms using a commercially available laser-based holography system. The short exposure time made possible by the laser overcomes the problem of blurring due to particle motion. The laser also provides a large coherence length which helps to maximize the depth of field for the holograms. Thus, using this technique with appropriate reconstruction of the holograms, particle size and number density information can be acquired as a function of shock tube radius, i.e., at selected planes along the line of sight. Of course, this three-dimensional imaging technique can also yield information on particle shape. The holographic technique is most useful for particle radii $\gtrsim$ 3 µm and scattering optical depths $\lesssim$ 0.1 (negligible multiple scattering); these constraints are generally consistent with the experimental conditions of present interest. The limitation, of course, will come in the assessment of particles in the 0.1 to 1 µm size range.

An alternative technique which has been proposed for particle sizing in the range of 0.02 $\lesssim$ a $\lesssim$ 1 µm is a laser-modulated-incandescence (LMI) technique (Ref. 31). Briefly, for the LMI method a short pulse laser operating at a wavelength strongly absorbed by the particle (ℓ_{abs} < r_p) is used to irradiate and heat a sample of the particle field. The time history of the resulting particle incandescence is then used to infer the particle dimensions. The particle size affects the particle's initial thermal equilibration by heat conduction and its subsequent cooling by radiation and heat transfer to the

surrounding medium. The advantage of this technique is that it is relatively easy to implement and can be used for assessing particle sizes in a regime inaccessible to many other in-situ optical techniques.

4.2.2 Diagnostic Options for Extinction, Emission, and Scattering Measurements

4.2.2.1 Radiation Sources for Extinction (and Scattering) Measurements

Line Sources - The sources considered in this category basically consist of a variety of commercial laser sources and atomic discharge lamps. In general, lasers are not needed for extinction measurements but make the task easier. On the other hand, lasers are virtually essential for performing angularly resolved scattering measurements with acceptable signal-to-noise levels.

In the category of atomic discharge lamps, one attractive option is to use a commercial hollow cathode discharge lamp with a stabilized power supply. For example a Hg or Hg-Cd lamp can provide approximately nine strong discrete lines distributed over the wavelength range of 300 to 580 nm with intensity levels more than adequate for making extinction measurements during the shock test time.

Commonly available commercial lasers are also useful and are essential if good quality, quantitative scattering data is to be obtained. Attractive candidate laser sources for these measurements are listed in Table 9.

Calculations of the optical signals that can be expected in a practical shock tube scattering measurement indicate that to achieve detectable scattering will require laser powers of at least a few milliwatts. This laser power requirement increases dramatically, however, if the particles to be probed are highly emissive and at high temperature. This is illustrated in Figure 47 where we have plotted the approximate laser power requirements for a scattering measurement at 1060 nm ($\Delta\lambda$ = 10 nm). For the purpose of the calculation, an acceptable scattering signal was assumed to be one for which the
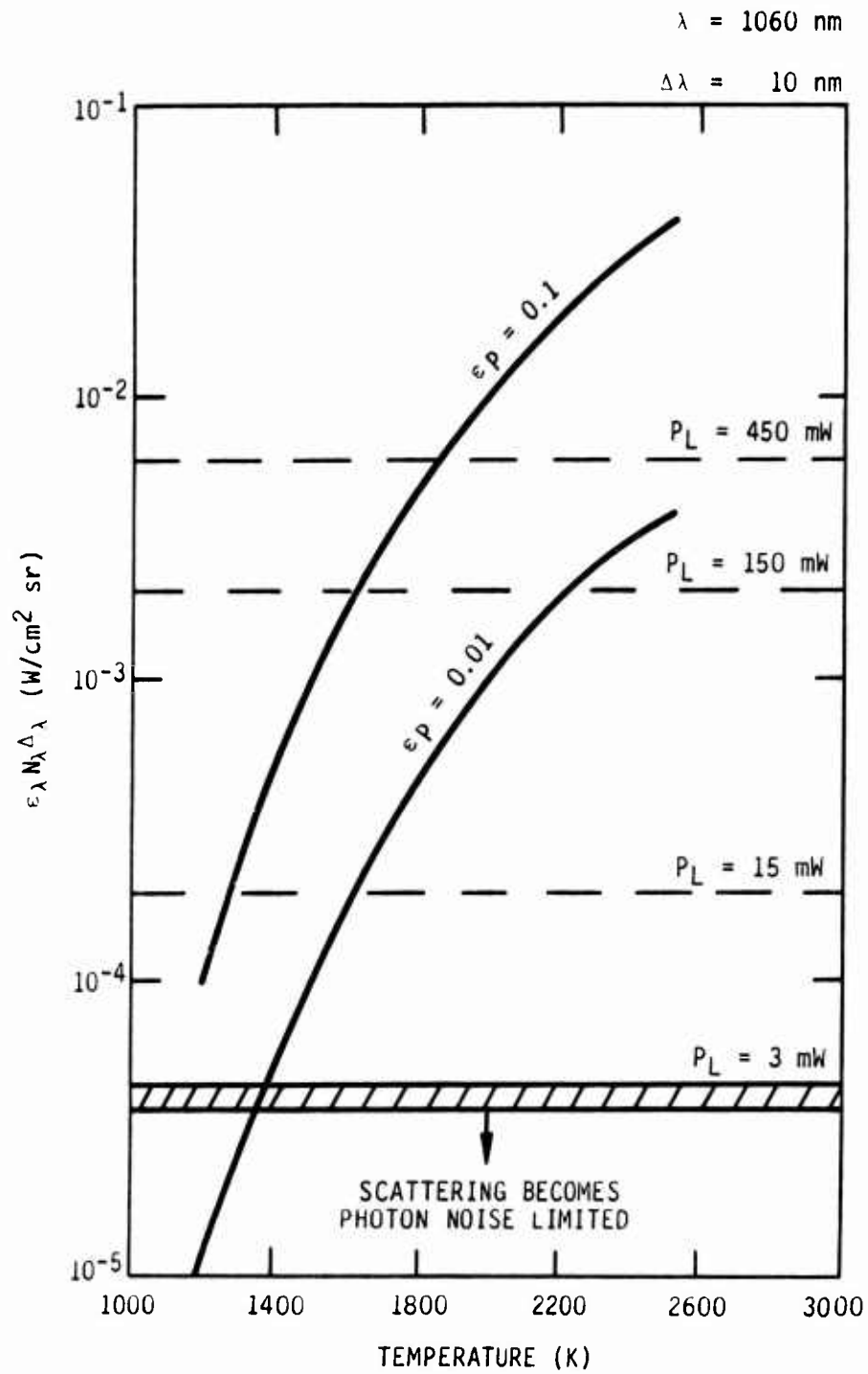
65

Figure 47. Approximate laser power requirements for scattering measurements ($P_{scatter} = 0.2\ P_{emission}$).

TABLE 9. Candidate Commercial Lasers Sources for Extinction
and/or Scattering Measurements.

Wavelength (μm)	Laser Type
0.458→0.515	Argon-ion
0.633	He-Ne
1.06	CW Nd:YAG or Glass
3.39	IR He-Ne
9.4→10.8	CW CO_2

signal is at least 20 percent of the background signal due to particle emission. The two solid curves in the plot represent the radiant emission that can be expected from the particles for different assumed values of the particle field emissivity (ϵ = 0.01 and ϵ = 0.1). As can be seen, for particle temperatures $\gtrsim$ 1400 K and ϵ $\gtrsim$ 0.01, the laser power requirements for a good scattering measurement increase dramatically with the particle temperature. For example, for T_P = 2500 K and ϵ = 0.01, the required laser power increases to nearly 300 mW.

In general, the problem of background particle emission will be even worse at longer wavelengths but can improve significantly when working at shorter wavelengths (such as at the 488 nm Ar-ion line). Figure 48 shows the results of calculations for the latter wavelength. Comparing Figures 47 and 48, one can clearly see the advantage of operating at the shorter wavelengths. For example, assuming a particle emissivity of 0.1 at both wavelengths and a temperature of 2200 K, we see that the laser power required for a scattering measurement decreases from approximately 1.5W at 1.06 μm to only ~50 mW at 490 nm.

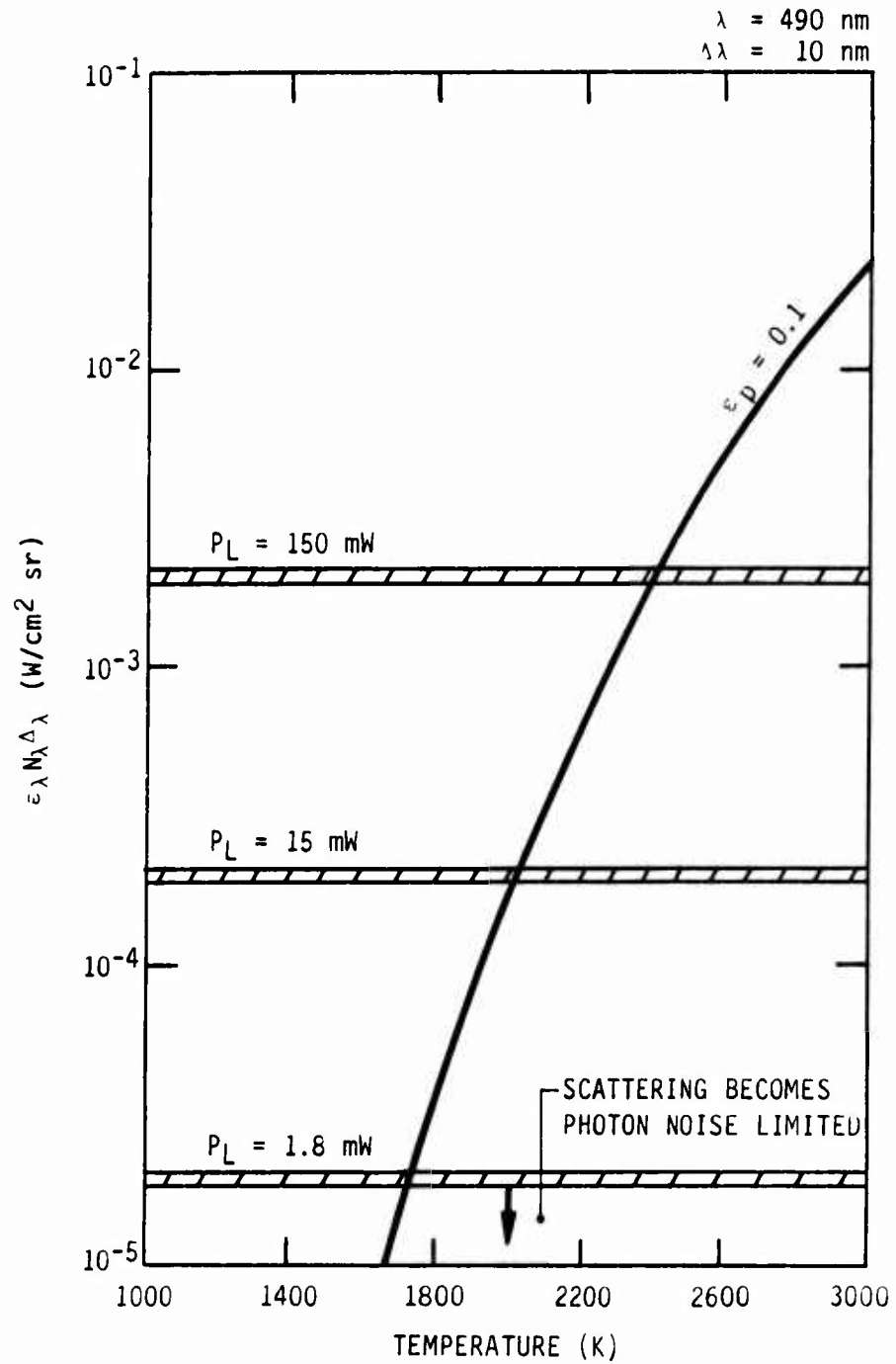Figure 48. **Approximate laser power requirements for scattering measurement** ($P_{scatter} > 0.2\ P_{emission}$).

68

In the final experiment design, similar calculations should be carried out for other laser wavelengths of interest and for a wider range of particle emissivities. In this way, acceptable operating regimes for scattering measurements can be clearly defined prior to hardware implementation and experimental testing.

Continuum Sources - In addition to using an array of discrete line sources for these experiments, it is also possible to make use of broadband continuum sources for performing the extinction measurements. For example, a good source for use in the wavelength range of 0.4 μm $\underset{\sim}{<} \lambda \underset{\sim}{<}$ 5 μm, would be a tungsten ribbon lamp equipped with a sapphire window. Such sources are commercially available, and can be operated with filament temperatures up to 2800 K. They routinely provide spectral radiances that start from approximately 5 μW/nm sr mm^2 at 0.4 μm, peak to $\sim$150 μW/sr mm^2 nm at approximately 1 μm, and then fall to about 3 μW/sr mm^2 nm at 4.5 μm. Assuming a solid angle collection factor of 3×10^{-2} sr (12° cone angle) and an effective filament area of $2 \times 6 = 12$ mm^2, these radiances yield availble spectral power densities of 1.7 μW/nm at 0.4 μm, 54 μW/nm at 1 μm, and 1.2 μW/nm at 4.5 μm. In all cases, such spectral power densities should be more than adequate for obtaining good quality shock tube extinction measurements. Scattering measurements, on the other hand, would be extremely problematic with such a source.

For wavelengths $\underset{\sim}{>}$ 4.5 μm, a standard large area blackbody calibration source ($T_{max} \approx$ 1000C) should be adequate for obtaining extinction data. For example, with T = 1250 K and a source emissivity = 1, the radiance at 4.5 μm is 5.4 μW/sr mm^2 nm. Assuming a source area = 50 mm^2 and $\Delta\Omega_{coll.} = 3 \times 10^{-2}$ sr, this yields an available spectral power density of 8.1 μW/nm. If the particle loading can be controlled so that the aerosol emissivity doesn't exceed 0.1, extinction signals that are measurable above the background emission should be measurable over the full temperature range of interest. In practice, the use of the 1000C blackbody source for extinction measurements might actually be feasible down to wavelengths as short as 2.5 microns.

4.2.2.2 Detection Schemes for Extinction, Scattering and Emission Measurements

Detection in the Near UV, Visible, and Near IR - One device that would be extremely useful for obtaining spectral information from the near UV to near IR ($\lambda < 1 \mu m$) in a single shock tube run is a gated-intensified diode array spectrograph (also known as an optical multichannel analyzer (OMA)). PSI currently owns such a device which can routinely be used to obtain spectra over the range from approximately 0.3 to 0.85 μm, with coverage on a single shot presently limited to a span of approximately 0.4 μm. With 0.4 μm coverage, the spectral resolution is $\sim 20\text{\AA}$. The image intensifier feature provides excellent sensitivity with overall quantum efficiencies corresponding to a response of 0.1 count-per-incident photon in the visible and UV. The gating option is also attractive as it allows time-resolved information to be obtained at selected delay times after shock passage. Detection time windows can routinely be varied from as short as 180 ns to up to 6 ms with controllable delay times from 270 ns to 7 ms. The maximum repetition frequency for obtaining spectra is 60 Hz. Thus, only one spectrum can be recorded during the available shock test time of a few milliseconds.

Despite this single spectrum limitation, the possibility may still exist to record extinction and emission spectra on a single shot. The approach would involve using a combination of discrete line sources to measure the extinction and superimposing these extinction signals upon the broadband emission spectrum. The procedure would be as follows: (1) before particle injection and shock initiation (and $\gtrsim$ 16 ms before shock passage) a spectrum of the transmitted intensity of the line source through the cold bath gas is recorded, (2) then, subsequent to particle dispersal and shock passage, another spectrum of the attenuated line spectrum is recorded superimposed on the broadband thermal emission spectrum from the shock-heated aerosol. A pictorial representation of the anticipated spectra is given in Figure 49.

Another approach to obtaining emission, extinction, (and scattering) data in the near UV to near IR is to use an array of dedicated photomultiplier
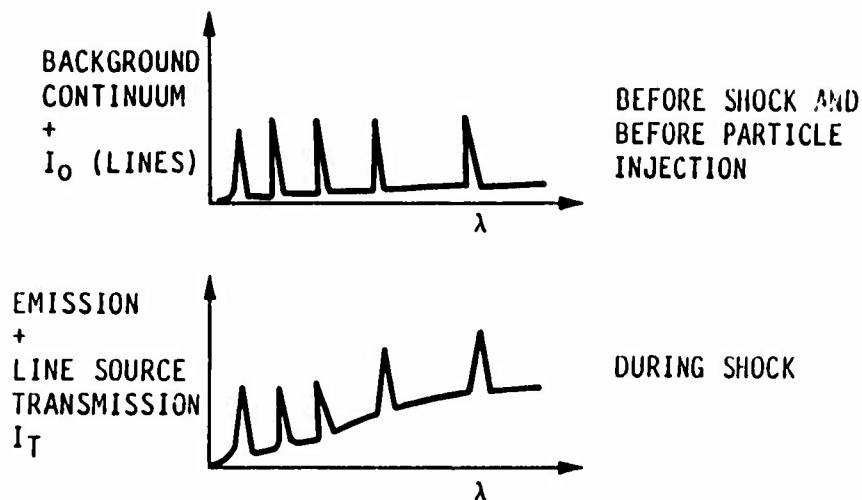
Figure 49. Anticipated OMA spectra for combined extinction and emission measurements.

tubes and/or solid state detectors each assigned to a fixed wavelength band-pass. With this detection scheme, simultaneous emission and extinction (or scattering) data can be obtained by high speed light choppers and various laser/line sources. The scheme is illustrated schematically in Figure 50 with a representation of the expected temporal waveform given in Figure 51.

The one advantage of this multiple independent detectors approach is that it provides a more complete time history of the aerosol extinction and emission behavior after shock passage. The disadvantage is that it requires many separate detector and data recording channels and provides less complete spectral coverage than the diode array spectrograph does. The best solution is perhaps to combine one or two independent emission/extinction bandpass detectors with the diode array spectrograph scheme described above.

Another spectral region of interest is, of course, the mid-IR ($\lambda \approx 2 \div 5$ μm). In this region, it is probably best to use a few dedicated InSb
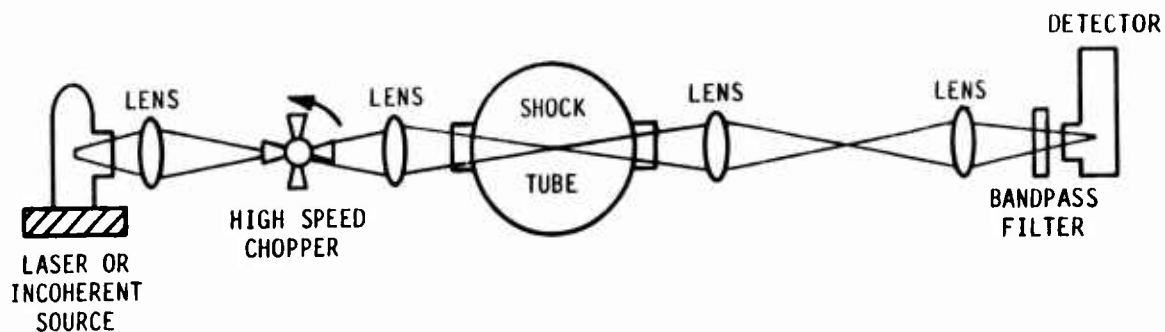
71

Figure 50. High speed chopping scheme for recording extinction and emission signals on a single detector.
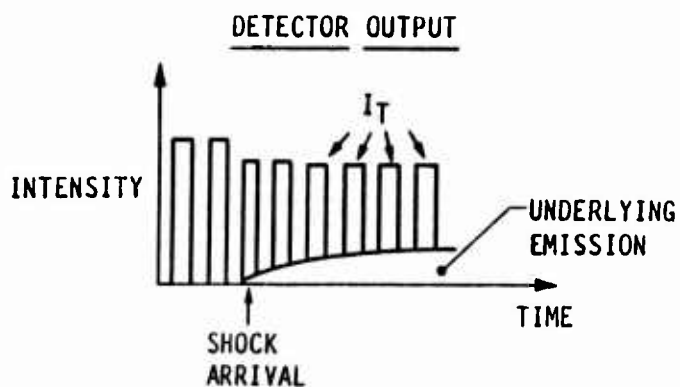

Figure 51. Anticipated temporal waveform with high speed chopping scheme for combined emission/extinction measurements in shock tube.

detectors each equipped with a different bandpass filter. Bandpass centers of interest might be, for example, 2.8, 3.39, 4.3 and 4.8 µm. The 3.39 µm bandpass is attractive because there is an IR He-Ne laser available at this wavelength which can be used to simultaneously measure extinction and emission. It may also be possible to use the tungsten ribbon lamp with sapphire window described earlier to measure extinction at other wavelengths.

The final wavelength regime of interest for the present measurements is what we will refer to here as the long wave IR region, or $\lambda \simeq 6$ µm $\rightarrow 12$ µm. For spectral coverage in this regime we recommend using a multielement linear array of liquid nitrogen cooled HgCdTe detectors coupled to a low resolution IR spectrograph. For example, with an eight element array it should be possible to obtain a spectrum from 6 to 11 µm in a single shot with a resolution of approximately 0.6 µm. Continuous spectral coverage in this wavelength regime appears to be important because of the onset of IR absorption bands for several of the materials of interest. Once again, for obtaining simultaneous extinction and emission data in this regime it should be possible to use a conventional blackbody source ($T_{max} = 1000°C$) with the high speed chopping technique described earlier. For the latter, the detector channels could be either multiplexed or read out independently. The latter would permit a full time history to be obtained for each wavelength channel.

5. CONCLUSIONS

After considering several potential techniques for producing the desired range of particle environments, we have chosen the shock tube method for the temperature range 1000 to 3000 K. While it is desirable to also obtain data between 300 and 1000 K, this temperature range is best achieved in a slow-flow, variable-temperature tube furnace.

The proposed experiments will be performed behind reflected shock waves in a 4-in. i.d. shock tube facility consisting of a driver section 4m in length and a modular test section 7.2m in length. Based on working times actually observed as well as times calculated from Rankine-Hugoniot relations, we expect working times ranging from 2.5 ms at 3000 K to 7.2 ms at 1000 K for a dilute suspension of particulates in Ar. These times are well in excess of the predicted times for convective/conductive heating and equilibration of 0.1 to 10 μm (radius) particles in Ar at 20 atm.

Prior to initiation of each shock wave experiment, selected particles will be dispersed into the observation volume near the end wall by means of a radial injection system. This approach offers several advantages over other methods which have proven successful in other "dusty" shock tube experiments. The injector will be capable of dispersing ~ 0.1g samples of particles uniformly into the optical field of view in a reproducible way. To insure adequate entrainment and mixing characteristics, the jet conditions will be optimized in bench tests using visiible light scattering to visualize the particle flow field.

The experimentally observed light extinction, particle emissivity, and scattered light angular distributions are directly related to the effective cross sections (or efficiency factors) for extinction, absorption, and scattering. These efficiency factors are in turn dependent on particle size and wavelength, and can be related to the complex refractive index at a given wavelength using Mie scattering theory.

74

The sensitivities of the observable extinction, absorption, and scattering/polarization parameters to their real and imaginary components have been discussed. From this analysis we have shown that ultraviolet extinction measurements may be used to determine particle number densities multiplied by cross-sectional area ($N_p \pi r^2$) with reasonable accuracy, while both extinction and emission become sensitive to refractive index of size parameter of 1.0. Once the quantity $N_p \pi r^2$ has been determined to within some error bound, then the quantities Q_E and Q_A can be determined at longer wavelengths to similar levels of accuracy. This in turn allows the determination of n and k, within appropriate error limits, from computed sensitivity curves.

Absolute scattering measurements are difficult to implement owing to: 1) the highly structured angular dependence for intermediate to large size parameter; 2) the need to calibrate the scattering/detection geometry in situ; and 3) the requirement for an intense laser source at each wavelength of interest. However, relative scattering measurements at two or more observation angles can be extremely important as a cross-check of the preshock particle size determinations and as a probe for agglomeration effects. Similarly, the polarization ratios of scattered light provide a sensitive test of particle shape effects.

Finally, the effects of particle size distribution and agglomeration have been shown to significantly affect the measured extinction and emission efficiencies. This effect mandates careful characterization of the particle size distribution for the experiments.

For the basic radiometric diagnostic approach, we recommend simultaneous measurements of: 1) light extinction at several selected wavelengths in the ultraviolet, visible, and infrared, using a variety of light source/ detector combinations; 2) spectrally resolved particle emission in the visible red and infrared, using calibrated radiometric and/or spectrometric detection schemes; and 3) laser scattering angular dissymmetry ratios and polarization/ depolarization ratios for confirmation of particle size and shape characteristics. Laser scattering and crossed-path extinction measurements will also

be used to characterize the spatial distributions of the dispersed particles in the reflected shock.

The recommended program of experimental measurements, coupled with the static rocket firing program at AFRPL, will lead to the development of a unique data base on particulate radiative properties which is sorely needed for predictive modeling of plume signatures. Possible extensions of this work would include more in-depth studies of the mechanisms influencing particulate formation and contamination in plumes, development of means for "tailoring" the particle radiation by manipulating these mechanisms, and application of our diagnostic methods to lower temperature measurements (300 to 1000 K) in a variable-temperature flow tube.

REFERENCES

1. Dowling, J.M., and Randall, C.M., Infrared Emissivities of Micron-Sized Particles of C, MgO, Al$_2$O$_3$, ZrO$_2$ at Elevated Temperatures, AFRPL-TR-77-14, The Aerospace Corporation, El Segundo, CA, April 1977.

2. Pluchino, A.B., Goldberg, S.S., Dowling, J.M., Randall, C.M., "Refractive-Index Measurements of Single Micron-Sized Carbon Particles." Applied Optics, 19, 19, pp. 3370-3372, 1980.

3. Mularz, E.J. and Yuen, M.C., "An Experimental Investigation of Radiative Properties of Aluminum Oxide Particles." Journal of Quantitative Spectroscopic Radiative Transfer, 12, pp. 1553-1568, 1972.

4. Adams, J.M., "A Determination of the Emissive Properties of a Cloud of Molten Alumina Particles." Journal of Quantitative Spectroscopic Radiative Transfer, 7, pp. 273-277, 1966.

5. Carlson, D.J., "Emittance of Condensed Oxides in Solid Propellant Combustion Products." Tenth Symposia (Int'l) on Combustion, pp. 1413-1424, 1965.

6. Nettleton, M.A., "Shock-Wave Chemistry in Dusty Gases and Fogs: A Review." Combustion and Flame, 28, pp. 3-16, 1977.

7. Konopka, W., Reed, R.A., Calia, V.S., Oman, R.A., Controlled Hot Gas/ Particle Experiments for Validation of a Standardized Infrared Radiation Model, Report No. AFRPL-81-44, Grumman Aerospace Corporation, Bethpage, New York, May 1981.

8. Calia, V.S., Konopka, W., Reed, R.A., and Omon, R.A., "Shock Tube Measurements of IR Radiation in Hot Gas/Particle Mixtures," Progress in A&A, 91, pp. 673-681, 1984.

9. Liepman, H.W. and Roshko, A., Elements of Gasdynamics, John Wiley and Sons, Inc., New York, 1965.

10. Gaydon, A.G., and Hurle, I.R., The Shock Tube in High-Temperature Chemical Physics, Reinhold Publishing Corporation, New York, 1963.

11. Cann, M.W.P., Shia, J.B., and Nicholls, R.W., "A Powder-Injection Shock-Tube Facility." 13th Shock Tube Symposia, pp. 98-106, 1981.

12. Lanzo, C.D., Measurement of the Transmissivity of a Carbon-Particle-Seeded Nitrogen Jet, NASA TN D-4722, NASA Lewis, Cleveland, OH, May 1986.

13. Harris, R.D., O'Dell, K., Pippin, G.G., Young, S.J., and Martin, L.R., Final Report: Study of Radiative Scattering Concept of Plume Infrared Radiation Obscuration, Contract No. F49620-77-C-0121. Utah State University, February, 1979.

14. Adamo, R.C., and Nunevicz, J.E., (1975), _Parametric Study of Electrostatic Techniques for Aerosol Dispersion_, Stanford Research Institute, Palo Alto, CA, March 1975.

15. Decker, L.J., Cohen, A., and Donnelly, E., _A Shock Tube Powder Dispersal Unit_, Report No. BRL-MR-3393, U.S. Army Ballistic Research Lab., Aberdeen Proving Ground, Maryland, October, 1984.

16. Lowenstein, A.I., and von Rosenberg, C.W., "Shock Tube Studies of Coal Devolatilization." Proceedings of the 11th International Symposia on Shock Tubes and Waves, pp. 366-374, Seattle, WA, July 1977.

17. Pai, S., _Fluid Dynamics of Jets_, D. Von Nostrand Company, New York, 1954.

18. Cetagen, B., Teichmon, K.Y., Weinberg, F.J., and Oppenheim, A.K., _Performance of a Plasma Jet Igniter_, Society of Automotive Engineers, Paper No. 80042, Warrendale, PA, 1980.

19. Longacre, P., Telephone conversation regarding particle delivery systems and agglomeration, MIT Lincoln Labs, Lexington, MA, December 1985.

20. van de Hulst, H.C., _Light Scattering by Small Particles_, Dover Publications, Inc., New York, 1981.

21. Kerker, M., _The Scattering of Light and Other Electromagnetic Radiation_, Academic Press, New York, 1969.

22. Dave, J.V., _Subroutines for Computing the Parameters of the Electromagnetic Radiation Scattered by a Sphere_, IBM Report No. 320-3237, IBM Scientific Center, Palo Alto, CA, May 1968.

23. Wyatt, P.J. and Stull, V.R., _Atlas of the Light Scattering Characteristics of Micro Particles_, Science Spectrum, Inc., Santa Barbara, CA, 1971.

24. Friese, G.J., Letter containing complex indices of refraction from 0.1 to 30 microns, Program Engineer, The Aerospace Corporation, San Bernadino, CA, 14 February 1972.

25. Dalzell, W.H., and Sarofim, A.F., "Optical Constants of Soot and Their Application to Heat-Flux Calculations." Transactions of the ASME, February 1969, pp. 100-104, 1969.

26. Lee, S.C. and Tien, C.L., "Optical Constants of Soot in Hydrocarbon Flames." 18th Symposium (Int'l) on Combustion, pp. 1159-1166, 1981.

27. Ludwig, C.B., Malkmus, W., Walker, J., Freeman, G.N., Reed, R., and Slack, M. (1981), _Standardized Infrared Radiation Model [SIRRM], Volume 1: Development and Validation_, Report No. AFRPL-TR-81-54, Photon Research Associates, La Jolla, CA, August, 1981.

28. Whitson, M.E., *Handbook of the Infrared Optical Properties of* Al_2O_3, C, MgO, *and* ZrO_2, Report No. SAMSO-TR-75-131, The Aerospace Corporation, El Segundo, CA, April 1975.

29. Parker, T.E., *Spray Ignition of Liquid Fuels of High Pressures and Temperatures and Thermodynamic Properties of Hydrocarbons*, Ph.D. Dissertation, Mechnical Engineering Department, University of California, Berkeley, April, 1985.

30. Pinnick, R.G., Carroll, D.E., and Hoffman, D.J., "Polarized Light Scattered from Monodisperse, Randomly Oriented, Non-Spherical Aerosol Particles: Measurements." *Applied Optics*, 15, 2, pp. 384-393, 1976.

31. Melton, L.A. (1984), "Soot Diagnostics Based on Laser Heating." *Applied Optics*, 23, pp. 2201-2208, 1984.